Civil Engineering Graduate Theses & Dissertations   Civil, Environmental, and Architectural Engineering

Spring 1-1-2012

Application of U-Series Disequilibria to Evaluate Fracture Flow and Fracture-Matrix Interactions at Pahute Mesa, Nevada National Security Site

Paul James Nichols
University of Colorado at Boulder, paul.nichols@colorado.edu

Follow this and additional works at: https://scholar.colorado.edu/cven_gradetds

Part of the Civil Engineering Commons, Geology Commons, and the Hydrology Commons

APPLICATION OF U-SERIES DISEQUILIBRIA TO EVALUATE FRACTURE FLOW AND

FRACTURE-MATRIX INTERACTIONS AT PAHUTE MESA, NEVADA NATIONAL

SECURITY SITE

by

Paul James Nichols

B.S., Washington State University, 2010

A thesis submitted to the

Faculty of the Graduate School of the

University of Colorado in partial fulfillment

of the requirement of the degree of

Master of Science

Department of Civil, Environmental and Architectural Engineering

This thesis entitled:
Application of U-series disequilibria to evaluate fracture flow and fracture-matrix interactions at
Pahute Mesa, Nevada National Security Site
Written by Paul James Nichols
Has been approved for the Department of Civil, Environmental, and Architectural Engineering

_____
Harihar Rajaram

_____
Roseanna Neupauer

_____
James B. Paces

Date_____

The final copy of this thesis has been examined by the signatories and we
Find that both the content and the form meet acceptable presentation standards
Of scholarly work in the above mentioned discipline.

Nichols, Paul James (M.S., Civil Engineering)
Application of U-series disequilibria to evaluate fracture flow and fracture-matrix interactions at Pahute Mesa, Nevada National Security Site
Thesis directed by Professor Harihar Rajaram

The U-Series decay chain was used to better understand groundwater movement through fracture networks on Pahute Mesa at the Nevada National Security Site. Whole rock core samples were taken from five boreholes on Pahute Mesa and were classified as either discrete fracture surfaces, or interior intact or brecciated/rubblized samples. After samples were chemically digested, a Thermo Finnigan Triton® mass spectrometer was used to determine $^{230}Th/^{238}U$ and $^{234}U/^{238}U$ A.R.s. It was determined that the majority of interior intact and brecciated/rubblized samples had A.R.s that clustered around secular equilibrium, while discrete fracture surfaces consistently had values that were more that 2% away from secular equilibrium. This reveals that groundwater flow on Pahute Mesa is dominated by discrete fracture networks. Rock interior samples at select distances away from discrete fracture surfaces were also collected and analyzed. Modeling attempts to capture the $^{230}Th/^{238}U$ and $^{234}U/^{238}U$ A.R.s at selected distances away from the discrete fracture surface were based on diffusion and were unsuccessful, as equation parameters were likely too unconstrained. Modeling samples' A.R.s relationships to the equiline was performed under steady state and transient conditions. This modeling approach was based on a balance between the influx and loss of ^{234}U and ^{238}U. Modeling results suggest that samples plotting on the equiline are at a steady state balance of ^{234}U and ^{238}U sources and sink terms. Samples plotting to the left of the equiline likely show that recent water-rock interaction has occurred and are representative of a U-adsorbing system. Given the uncertainty of the input and loss rates of U nuclides, many different scenarios were generated to explain samples' relationships to the equiline.

ACKOWLEDGEMENTS

First of all, I would like to thank the Department of Energy for funding the research that developed into this master's thesis. The Department of Energy's commitment to safeguarding groundwater for human use is of vital importance as we seek a future balance between energy experimentation and development and the continued welfare and safety of the public. I would also like to thank Dr. James Paces of the USGS for directly supplying funding for this project, for his commitment to tedious data collection, for his continuous enthusiasm for teaching me geological and geochemical concepts and experimental techniques, and for his appreciation for the differences between scientists and engineers that often arose in project discussions and debates. I would also like to thank Dr. Leonid Neymark of the USGS for his valuable and meticulous insight and scrutiny throughout the scope of this project. Additionally, I would also like to thank my adviser, Dr. Harihar Rajaram who, through rigorous coursework and this thesis project, has shaped my knowledge of flow and transport of solutes in our environment and greatly improved my previous knowledge in mathematics. His commitment to complementing my mathematical short comings and his willingness to devote substantial time to enable me to complete this thesis on my time scale is greatly appreciated. I would also like to acknowledge Dr. Roseanna Neupauer for her commitment to improving my understanding and analytical skills in groundwater as it applies to civil engineering. Her genuine fervor to see all undergraduate and graduate students alike succeed will help to ensure the quality of the Hydrology, Water Resources, and Environmental Fluid Mechanics program at University of Colorado.

Lastly, but certainly not least, I would like to thank my parents and siblings for their unwavering love and support. Without their financial, emotional, intellectual, and time

commitments to me, my graduate career and this thesis would not have been possible. Spur of the moment trips between Boulder and Toppenish, and frequent and often haphazard phone calls, texts, and e-mails have made the biggest difference in my life over these last two years and have allowed me to get to where I am today.

 THANK YOU

CONTENTS

TABLES

FIGURES

CHAPTER 1

INTRODUCTION

This research was motivated by a need to better characterize the complex

hydrogeological features that govern groundwater flow on the Pahute Mesa, located in

Administrative Areas 19 and 20 of the Nevada National Security Site (NNSS), formerly the

Nevada Test Site. This is a high priority for the United States Department of Energy, which is

concerned with groundwater flow rates and flow paths as a means of dispersing radionuclides

derived from nuclear weapons testing and their potential adverse impacts on human health. This

thesis focuses on fractures that provide secondary permeability through volcanic units and

investigates the distribution of fractures indicating recent groundwater flow using uranium-series

isotopes as sensitive indicators of water-rock interaction. Past research has shown that U-series

disequilibrium is a useful tool for investigating the presence of groundwater at the NNSS.

Specifically, this technique has been used to characterize the unsaturated zone at Yucca

Mountain (Neymark, et al., 2006; Paces, et al., 2002; Paces, et al., 2006) and to understand

groundwater in the saturated zone on the NNSS (Copenhaver, et al., 1992). From U-series

analysis, we expect to be able to characterize select pieces of core as being taken from regions of

flowing groundwater or from regions were groundwater is either stagnant or nonexistent.

Work included core selection from the Mercury Core Library in Mercury Nevada,

chemical and radiological preparation and testing of core samples, and efforts to model the

hydrological processes that corresponded to the uranium (U) and thorium (Th) series data.

Sample collection included discrete fracture, brecciated/rubblized, and interior rock samples.

Also, samples at select intervals into the bulk rock from discrete fracture surfaces were analyzed.

Modeling efforts were first focused on characterizing diffusive processes that govern water flow perpendicular to discrete fracture surfaces into bulk rock matrix. It was later determined that chemical and physical parameters governing this process were too unconstrained for the scope of this thesis project. Consequently, no reasonable results were obtained using this approach. Modeling efforts then focused on employing well-mixed system behavior providing a basis to better understand the distribution of observed $^{234}U/^{238}U$ and $^{230}Th/^{238}U$ A.R.s in discrete fracture samples, especially with respect to their position along the equiline, defined as the relationship where $^{234}U/^{238}U$ A.R. = $^{230}Th/^{238}U$ A.R. Points that lie on the equiline likely represent a steady state balance between radionuclide gain and loss whereas points plotting off of the equiline are indicative of transient relationships between the sources and sinks of radionuclides. This thesis presents qualitative and quantitative simulations that potentially explain the observed isotopic behavior of the data set and offers possible hydrologic and geochemical explanations relevant to groundwater flow and transport.

It is the author's hope that the progress in characterizing groundwater flow at Pahute Mesa will better enable the United States Department of Energy, in collaboration with the United States Geological Survey, to implement solutions to safeguarding the domestic water supply. It is also the author's hope that work highlighted in this thesis can be used to develop more constrained models of fracture flow on Pahute Mesa and can ultimately lead to groundwater flow models that rely on discrete fracture networks in the regional aquifer system.

CHAPTER 2

SITE BACKGROUND

The NNSS (Figure 2-1) is located approximately 90 miles northwest of Las Vegas, Nevada and is characterized by a very hydrogeologically diverse 1,350 square mile terrain in south central Nevada (Lacziak et al., 2005). The geology of the NNSS is highly complex, consisting of thick volcanic tuffs and lavas of Cenozoic age overlying basement rocks consisting of Paleozoic limestone, dolomite, shale, and Precambrian quartzite (Fenelon et al., 2010). Compressional tectonic forces during the Mesozoic and late Cenozoic extension have resulted in structural juxtaposition of rock units as well as basins filled with thick alluvial deposits. The complex geology of the NNSS has been grouped into hydrostratigraphic units on the basis of rock types and permeability resulting in aquifer units, confining units, and composite units that may contain hydraulic characteristics of aquifers and confining layers depending on the nature of the individual strata within the unit (Fenelon et al., 2010). Hydrostratigraphic units may include the effects of localized metamorphism and mineralization, tectonic fracturing, hydrothermal alterations, and underground nuclear testing (Fenelon et. al, 2010).

From the 1950's to 1992 (Drellack and Ortego, 2007), the NNSS was used for conducting underground tests of numerous nuclear devices (Lacziak et al., 2005). After enactment of the Limited Test Ban Treaty of 1963, testing at the NNSS was restricted to nuclear detonation below the land surface. In an effort to contain radioactive contaminates and prevent atmospheric pollution, the majority of the large yield tests were detonated below the water table, which ranges from 865 ft to 2,345 ft below the land surface on Pahute Mesa (Blankennagel and Weir, 1973). In total, 921 nuclear devices were detonated below the land surface, many of them on

Pahute Mesa (total of 85), a volcanic plateau in the northwestern portion of the test site (Fenelon et al., 2010). Specifically, Pahute Mesa is located in Administrative Areas 19 and 20 of the NNSS and ranges in elevation from 5,500 ft to 7,000 ft, with elevation being the highest in the eastern portion of NNSS Administrative Area 19 (Figure 2-1). At Pahute Mesa, 90% of the detonation experiments occurred below the water table. A total of 80 tests were conducted at depths sufficient to emplace radioactive contaminants directly into the regional groundwater flow system (Lacziak et al., 2005). This has resulted in the contamination of the highly complex regional groundwater flow system (Lacziak et al., 2005). The likelihood that the long-lived radioactive isotopes generated during these tests eventually will be mobilized provides motivation for further understanding the movement of groundwater on the NNSS.

The NNSS is located in the Death Valley groundwater flow system. An estimated 70,000 acre-feet per year of groundwater flows through the system mostly in carbonate and volcanic aquifers away from areas of recharge in the north, towards discharge areas in the south at Ash Meadows, Oasis Valley, Alkali Flat, and Death Valley. Specifically, Pahute Mesa is part of the Oasis Valley and the Alkali Flat flow systems (Lacziak et al., 2005). There is a concern that radionuclide contamination from Pahute Mesa will enter Thirsty Canyon and ultimately reach the discharge sites in Oasis Valley and enter the Amargosa River (Reiner et al., 2002). While most of the groundwater flow on Pahute Mesa is derived from local recharge, it is acknowledged that some portion of the total groundwater flow through Pahute Mesa likely comes from north of the NNSS boundary and flows southward towards the Oasis Valley (Fenelon et al., 2010). Estimates of the groundwater flow rates at Pahute Mesa vary greatly from less than 7 ft/yr to more than 250 ft/yr and are highly dependent on the extent of fracturing, secondary mineralization/zeolitization, and lithology, with fracture networks providing for the possibility of high secondary

permeability. Lava flows and highly fractured welded ash-flow tuffs form aquifer units at Pahute

Mesa, while non-welded ash-fall tuffs generally form confining units (Lacziak et al., 2005). Due

to the high degree of fracturing seen in the rock units at Pahute Mesa, secondary permeability

associated with fracture networks in the rock matrix is of great significance to groundwater flow,

and thus the transport of radioactive nuclides on Pahute Mesa (Lacziak et al., 2005). This

provides motivation for investigating the nature of flow through Pahute Mesa by analyzing

discrete fracture surfaces from borehole core samples from Administrative Areas 19 and 20 on

the NNSS.

In order to select appropriate samples, it was necessary to identify existing core located

below the water table. The characterization of the potentiometric surface at Pahute Mesa was

complicated by the presence of recharge-fed localized perched water tables overlaying confining

units. Mean values of pre-testing hydraulic heads from 800 wells on the NNSS were used to

create potentiometric contours across the entire NNSS, providing a basis for the characterization

of the water table on Pahute Mesa (Fenelon et al., 2010). This information was used to select five

bore holes that had preserved drill core from both aquifer and confining units below the

established regional water table. Figure 2-1 shows the locations of the selected bore holes in

Administrative Areas 19 and 20.
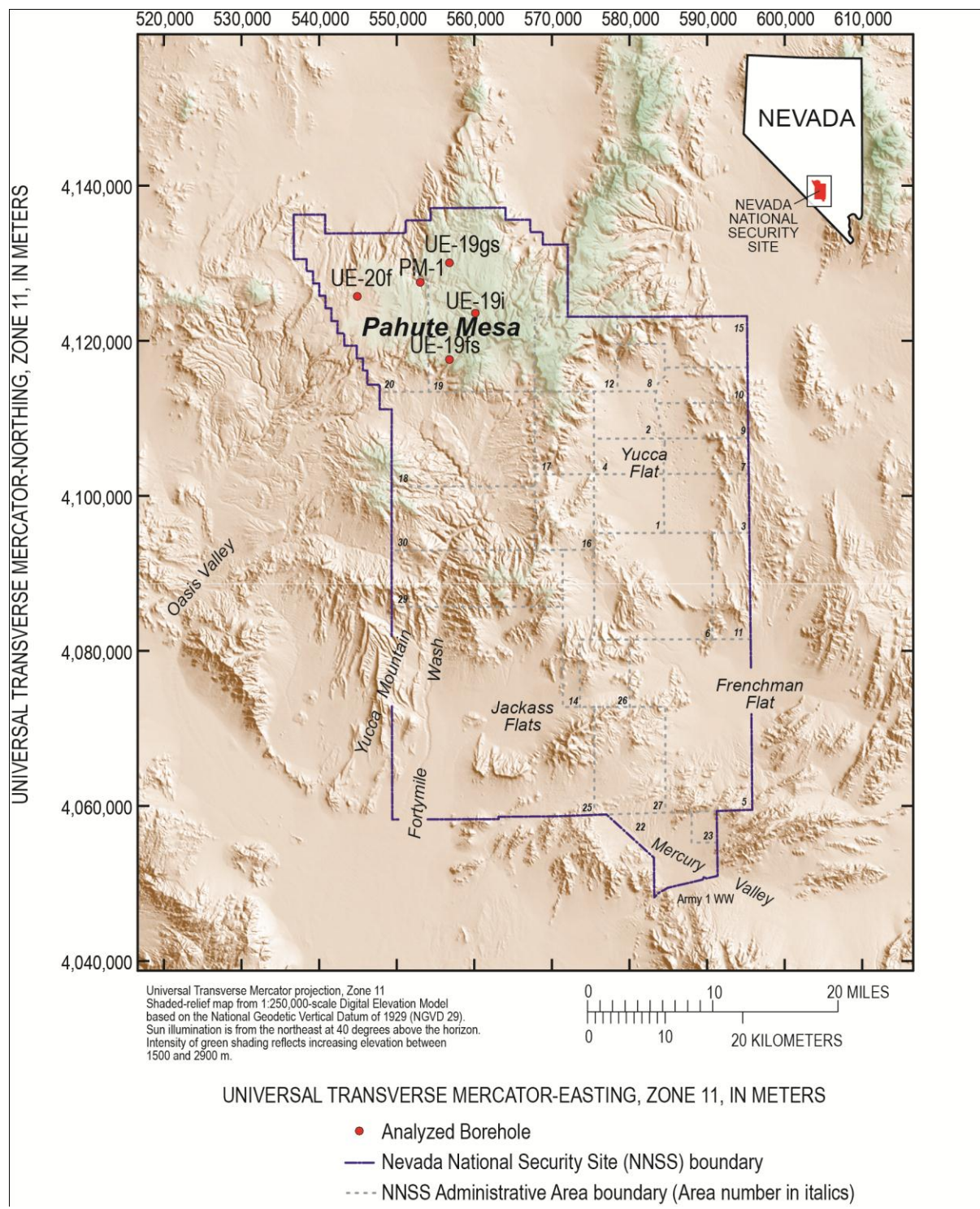
Figure 2-1. Location of Nevada National Security Site and boreholes analyzed in this research project

CHAPTER 3

U-SERIES APPROACH TO THE PROBLEM

In order to better characterize the transport of radionuclides through Pahute Mesa, the uranium-series decay chain was explored. The U-series decay chain includes a number of radioactive isotopes that represent decay products starting from the natural radionuclide ^{238}U, ultimately resulting in a production of stable isotope of lead,^{206}Pb (Krishnaswami et al., 1982). Intermediate radioactive daughter products with relatively long half-lives are important for investigating hydrogeologic processes. Both ^{234}U and ^{230}Th isotopes are derived from spontaneous alpha-decay with half-lives of 2.47E05 years and 7.7E04, respectively (Fauer, 1986).The use of ^{234}U/^{238}U and ^{230}Th/^{238}U isotopic ratios has become an important tool in the investigation of interactions between aquifer rock matrix and migrating groundwaters (Chabaux et al., 2008; Porcelli and Swarzenski, 2003; Procelli, 2008; Tricca et al., 2000). U-series isotopes in rocks which have remained closed to chemical exchange with their surrounding will attain a state of radioactive secular equilibrium where the decay of all daughter products is dependent on the rate of decay of the much longer-lived parent, ^{238}U (Fauer, 1986; Gascoyne and Miller, 2000). At this point, the radioactivity of ^{230}Th is equal to that from ^{234}U, which is equal to that from ^{238}U. Since ^{238}U and ^{234}U are present in all ground waters and have unique half-lives, groundwater processes governing their isotopic ratios over differing time scales can be investigated (Porcelli and Swarzenski, 2003). Due to the small amount of measurable ^{238}U, ^{234}U, and ^{230}Th nuclides, ratios of the radioactive isotopes are sought and analyzed (Chabaux et al., 2008). These ratios are expressed as activity ratios (A.R.s) where the activity of a particular nuclide is defined as the nuclide's concentration multiplied by the nuclide's decay constant.

In contrast, rock matrix samples that have been recently exposed to flowing groundwater exhibit radionuclide A.R.values that differ significantly from 1.0 (Neymark et al., 2006). This is likely due to water-rock interaction (adsorption-desorption or dissolution-precipitation) and groundwater transport of the more soluble nuclides (Gascoyne and Miller, 2000). Therefore, U-series disequilibrium provides a way to verify that intact rock has not seen any interaction with water, characterize groundwater flow through aquifers and matrix fracture networks, and ultimately determine the potential mobility of radionuclide contaminants in groundwater.

Water-rock interaction typically results in preferential loss of ^{234}U with respect to ^{238}U, due to the effect of the alpha-recoil process (Chabaux et al., 2008; Deschamps et al., 2004; Gascoyne and Miller, 2000; Osmond and Cowart, 1992). In addition, U from the rock is lost to groundwater with respect to Th, due to much greater chemical solubility of U relative to highly insoluble Th. As a result, minerals precipitating from groundwater on fracture surfaces during groundwater flow will typically contain ^{234}U/^{238}U A.R. > 1.0 and extremely low ^{230}Th/^{238}U A.R. approaching zero. To balance this process, the remaining rock will shift slightly towards lower values of ^{234}U/^{238}U A.R. (i.e., <1.0) and higher values of ^{230}Th/^{238}U A.R. (Latham and Schwarcz, 1987). Over long periods of time, these slight shifts can result in U-series isotopic composition in the rock that are measurably distinct from secular equilibrium.

The degree of the disequilibrium observed in rock matrix samples is dependent on a host of physical and chemical processes, including porosity, surface area, water content, groundwater flow velocities, weathering rates, U concentrations, and absorption (Paces et al., 2006).

CHAPTER 4

SAMPLE SELECTION AND PREPARATION

For this study of saturated zone fractures at Pahute Mesa, sample selection was based on

the availability of drill core in the saturated zone archived at the USGS Mercury Core Library,

located in Mercury, Nevada. The nature and availability of drill core was determined using the

Mercury Core Library online database. The availability of drill core, as opposed to cuttings, was

essential in order to perform U-series analysis on discrete fracture surfaces. Boreholes from

Pahute Mesa that were selected for analysis were: UE-19i, UE-19gs, UE-19fs, UE-20f, and

PM-1. The locations of the boreholes, shown in Figure 2-1, are as follows: 37.2246N, -

116.3684W (UE-19fs); 37.3082N, -116.3655W (UE-19gs); 37.2499N, -116.3478W (UE-19i);

37.2714N, -166.4888W (UE-20f); and 37.2802N, -166.4068W (PM-1). Depths to the modern

static water table have been measured in these boreholes (Fenelon et al., 2010) with values of

2341 ft (UE-19i), 2043 ft (UE-19gs), 2302 ft (UE-19fs), 1953 ft (UE20f), and 2144 ft (PM-1)

below the land surface. These approximate locations of the water table on Pahute Mesa represent

the potentiometric surface, rather than perched water tables, which, as previously noted, are

prominent throughout the mesa due to localized points of precipitation-induced recharge

(Fenelon et al., 2010). All samples selected for this study were from well below the lowest

reported water levels.

Samples targeted for analysis consisted of several different physical types including

discrete fracture surfaces, intact core, and brecciated/rubblized (highly broken) zones from both

aquifer and confining units. In the sample selection process, both aquifer and confining units as

defined by Fenelon et al. (2010) were targeted so that disequilibrium results for discrete fracture

surfaces in different hydrogeologic settings could be analyzed. Specifically, hydrogeologic unit designations for the various rock units in the analyzed boreholes followed properties based on their hydrostratigraphic classification and included aquifer units, confining units, and composite units which can behave as either aquifer or confining units depending on properties that vary on either lateral or stratigraphic scales.

Before traveling to the Mercury Core Library in Mercury, Nevada, previously selected aquifer units were analyzed using available photographs of selected core boxes and fracture descriptions based on Wood (2009). These findings were then verified by visual examination of core at the Mercury Core Library in March 2011 during a sample collection and site visit to the NNSS. Table 4-1 below lists the samples that were selected from the Mercury Core Library and shipped to USGS laboratories in Denver. The table also shows the naming convention used throughout this report. Samples were named according to the borehole name and the top depth of the interval selected. A left and right parenthesis was used to distinguish between a discrete fracture surface and a brecciated/rubblized or interior intact core taken from the same depth interval. A further explanation on of the hydrostratigraphic units listed in Table 4-1 is given in the Appendix.

Table 4-1. Whole Rock Sample Selection and Characterization

Borehole Name	Hydrostratigraphic Unit Abbreviation	Unit Type	Interval (ft from land surface)	Sample Name	Sample Treatment
UE-19fs	CHCU (Tuff)	Confining	2553.9-2554.2	UE19fs-2554	Discrete Fracture
UE-19fs	IA (Rhyolite)	Aquifer	3375.0-3375.3	UE19fs-3375	Discrete Fracture
UE-19fs	IA (Rhyolite)	Aquifer	3552.1-3552.5	UE19fs-3552	Discrete Fracture
UE-19fs	IA (Rhyolite)	Aquifer	4303.1-4303.5	UE19fs-4303	Discrete Fracture
UE-19fs	BFCU (Tuff)	Confining	4913.3-4913.7	UE19fs-4913	Discrete Fracture
UE-19fs	BRA (Rhyolite)	Aquifer	5211.4-5121.0	UE19fs-5211	Discrete Fracture

UE-19fs	BRA (Rhyolite)	Aquifer	5214.5-5214.7	UE19fs-5242	Discrete Fracture
UE-19fs	BRA (Tuff)	Aquifer	5516.6-5516.8	UE19fs-5517()	Discrete Fracture
UE-19fs	BRA (Tuff)	Aquifer	5516.6-5516.8	UE19fs-5517	Brecciated/Rubblized
UE-19fs	BRA (Rhyolite)	Aquifer	5815.6-5815.9	UE19fs-5816()	Discrete Fracture
UE-19fs	BRA (Rhyolite)	Aquifer	5815.6-5815.9	UE19fs-5816()	Brecciated/Rubblized
UE-19gs	BRA (Rhyolite)	Aquifer	2136.0-2136.6	UE19gs-2136()	Discrete Fracture
UE-19gs	BRA (Rhyolite)	Aquifer	2136.0-2136.6	UE19gs-2136	Brecciated/Rubblized
UE-19gs	BRA (Shard Tuff)	Aquifer	4054-4057	UE19gs-4054()	Discrete Fracture
UE-19gs	BRA (Shard Tuff)	Aquifer	4054-4057	UE19gs-4054	Brecciated/Rubblized
UE-19gs	BRA (Tuff)	Aquifer	4657.5-4657.9	UE19gs-4658()	Discrete Fracture
UE-19gs	BRA (Tuff)	Aquifer	4657.5-4657.9	UE19gs-4658	Brecciated/Rubblized
UE-19gs	BRA (Tuff)	Aquifer	4814.3-4814.5	UE19gs-4814	Interior Intact
UE-19gs	BRA	Aquifer	4907.8-4908.0	UE19gs-4908()	Discrete Fracture
UE-19gs	BRA	Aquifer	4907.8-4908.0	UE19gs-4908	Brecciated/Rubblized
UE-19gs	BRA (Tuff)	Aquifer	5302.5-5302.8	UE19gs-5303	Discrete Fracture
UE-19gs	BRA (Tuff)	Aquifer	5641.0-5641.4	UE19gs-5641	Discrete Fracture
UE-19gs	BRA (Tuff)	Aquifer	6279.0-6279.3	UE19gs-6279()	Discrete Fracture
UE-19gs	BRA (Tuff)	Aquifer	6279.0-6279.3	UE19gs-6279	Brecciated/Rubblized
UE-19i	CFCU (Tuff)	Confining	2419.0-2419.2	UE19i-2419	Interior Intact
UE-19i	BFCU (Tuff)	Confining	2890.5-2890.6	UE19i-2891	Discrete Fracture
UE-19i	BFCU (Rhyo-Breccia)	Confining	3407.0-3407.2	UE19i-3407()	Discrete Fracture
UE-19i	BFCU (Rhyo-Breccia)	Confining	3407.0-3407.2	UE19i-3407	Brecciated/Rubblized
UE-19i	BFCU (Tuff)	Confining	3533.0-3533.3	UE19i-3533()	Discrete Fracture
UE-19i	BFCU (Tuff)	Confining	3533.0-3533.3	UE19i-3533	Brecciated/Rubblized
UE-19i	BFCU	Confining	3815.0-38151.2	UE19i-3815	Interior Intact
UE-20f	LPCU	Confining	2848.7	UE20f-2849	Discrete Fracture
UE-20f	TCA	Aquifer	2626.275-2626.4	UE20f-2626	Discrete Fracture
UE-20f	LPCU	Confining	2845.4-2845.6	UE20f-2845	Discrete Fracture
UE-20f	CHZCM (Tuff)	Composite	3030.4-3030.6	UE20f-3030()	Discrete Fracture
UE-20f	CHZCM (Tuff)	Composite	3030.4-3030.6	UE20f-3030	Brecciated/Rubblized
UE-20f	CHZCM (Vitrophyre)	Composite	3607.3-3607.4	UE20f-3607	Discrete Fracture
UE-20f	CHZCM (Tuff)	Composite	3704.4-3704.7	UE20f-3704	Discrete Fracture
UE-20f	CHZCM (Tuff)	Composite	3904.2-3904.3	UE20f-3904	Interior Intact
UE-20f	CHZCM (Tuff)	Composite	4159.8-4160.0	UE20f-4260	Interior Intact
UE-20f	IA	Aquifer	4740.7-4741.0	UE20f-4741	Discrete Fracture
UE-20f	IA	Aquifer	5290.7-5291.0	UE20f-5291	Discrete Fracture
PM-1	CHZCM	Composite	1990.0-1990.15	PM1-1990	Discrete Fracture
PM-1	CHZCM (Tuff)	Composite	2366.4-2366.6	PM1-2366	Discrete Fracture
PM-1	CHZCM (Tuff)	Composite	2820.5-2820.6	PM1-2821	Interior Intact
PM-1	CFCU (SNDS)	Confining	3140.5-3140.7	PM1-3141	Interior Intact
PM-1	BFCU (Tuff)	Confining	3456.4-3456.6	PM1-3456	Interior Intact
PM-1	BRA (Tuff)	Aquifer	5597.5-5597.7	PM1-5598	Discrete Fracture
PM-1	BRA (Tuff)	Aquifer	5779.6-5779.9	PM1-5780	Discrete Fracture

PM-1	BRA (Tuff)	Aquifer	5996.5-5996.8	PM1-5997	Discrete Fracture
PM-1	BRA (Tuff)	Aquifer	6079.0-6079.2	PM1-6079()	Discrete Fracture
PM-1	BRA (Tuff)	Aquifer	6079.0-6079.2	PM1-6079	Brecciated/Rubblized
PM-1	BRA (Tuff)	Aquifer	6084.0-6084.3	PM1-6084	Discrete Fracture
PM-1	BRA (Tuff)	Aquifer	6614.0-6614.2	PM1-6614	Interior Intact

The following photographs display a small selection of core samples from the Mercury Core Library and show an example of core from borehole PM-1 stored in cardboard core boxes including discrete fracture surfaces, brecciated/rubblized core fragments, and interior intact core.

Figure 4-1. Box of drill core from borehole PM-1 at the USGS Mercury Core Library showing samples of a discrete fracture at 6084' and brecciated/rubblized core at 6079'

Figure 4-2. Box of drill core from the USGS Mercury Core Library showing a sample of interior intact core at 6614'

In selecting discrete fracture surfaces, we sought natural looking fractures with the appearance of secondary mineral surfaces coatings in order to eliminate fractures that may have been induced by the drilling process. Back in the laboratory, selected discrete fracture surfaces were then scrapped with a carbide dental drill bit in order to obtain 100 to 130 mg of rock powder for later chemical digestion in order to prepare the sample for U-series analysis. Relatively large areas (up to 4,000 mm^2) were scraped in order to minimize the thickness of the outermost layers included in the sample (typically less than 0.2 mm). Figure 4-3 shown below illustrates the selection of a naturally occurring fracture surface before and after scrapping with a carbide dental drill bit. Careful effort was made to minimize the amount of whole rock that was scraped in order that the sample would bear the signature of the fracture surface rather than the underlying whole rock.

Figure 4-3. Illustration of discrete fracture before and after scraping for PM-1:6084'

Sampling of the interior intact and brecciated/rubblized core was approached in a different manner. These samples were crushed to approximately 3 mm or finer, and then cone and quartered (Schumacher et al., 1991), resulting in a homogenous representation of the bulk

material. Approximately 20 grams of rock fragments were subsequently placed in a steel shatter box and pulverized to less than 75μm. This resulted in a fine powder from which 100 to 130 mg was selected for later chemical digestion. This is consistent with sample selection amounts from previous studies (Paces et al., 2006). In order to purify the small amounts of U and Th contained in the rock samples, all samples were digested using the techniques outlined in Weis et al. (2006). Techniques used to isolate U and Th isotopes are also similar to those discussed outlined in previous studies in (Paces et al., 2002; Paces et al., 2006).

Aliquots of rock powder were weighed in 15 ml Teflon beakers and combined with 0.5 ml of 15 Normal (N) nitric acid (HNO_3) and 3.0 milliliters (ml) of 48% concentrated hydrofloric acid (HF), capped tightly, cooked overnight at 135ºC, and then dried down. All samples were then combined with 0.5 ml 15 N HNO_3 and 0.5 ml 9 N hydrochloric acid (HCl) and heated on a 135ºC hotplate for two hours before being dried down. 5 ml of 6.5 N HCl was then added to all beakers and samples were allowed to equilibrate on a 130ºC hotplate overnight. Samples were then transferred as 5 ml 6.5 N HCl into 15 ml centrifuge tubes and then spun at 10,000 rpm for 10 minutes. If gel was visible after samples were spun down, samples were further digested with 9 N HCl and 15 N HNO_3 until all gel was dissolved. After complete chemical digestion of samples, acid solutions were split into two separate aliquots, one of which was weighed and spiked with approximately 0.0400 grams of a mixed $^{236}U/^{229}Th$ tracer, allowed to equilibrate overnight on a hot plate, and then dried down and redissolved in 1 ml of 7 N HNO_3.

In order to obtain the purified separates of U and Th, spiked sample solutions were loaded into clean columns containing 1 ml of BioRad AG 1x8 200-400 Mesh anion-exchange chromatographic resin as 1 ml 7 N nitric. Th was then eluted from the columns into clean Teflon beakers using 6.5 N HCl. Then U was eluted from columns after switching to the original 15 ml

beakers using 0.05 N HNO_3. A detailed description of the sample purification procedures can be viewed in the Appendix.

U and Th isotopic ratios were then determined using thermal ionization mass spectrometric methods similar to those discussed elsewhere (Paces et al., 2002; Paces et al., 2006). Purified U and Th salts were loaded onto the low-temperature sides of double Rhenium filaments assemblies using 6.5 N HCl and analyzed on a ThermoFinnigan Triton® mass spectrometer equipped with an ion counting system and a retarding potential quadrapole (RPQ) energy filter. Ratios of $^{234}U/^{235}U$, $^{236}U/^{235}U$, $^{230}Th/^{229}Th$, and $^{232}Th/^{229}Th$ were measured using a single electron multiplier operating in a peak jumping mode. International isotope standard NIST SRM-4321 was loaded as a means to analyze the accuracy and precision of the mass spectrometer's reported measurements. The resulting isotopic data is shown in Chapter 5.

CHAPTER 5

CHEMICAL RESULTS

Whole Rock Results

Table 5-1 and Figures 5-1 and 5-2 on the following pages show the whole rock results that were obtained using a ThermoFinnigan Triton® mass spectrometer as described in Chapter 4. As indicated in Table 5-1, isotopic ratios were measured to be accurate to the nearest 0.0000 activity while nuclide concentrations were measured to be accurate to the nearest 0.00 part per million.

Table 5-1. Whole rock U-series results

Sample ID	Borehole	Depth (ft)	Sample Type	Date	U (ppm)	±2s	Th (ppm)	±2s	^{230}Th/^{238}U AR	±2s	^{234}U/^{238}U AR	±2s
PM1-2366 ()	PM-1	2366	Discrete Fracture	40725	2.54	0.09	10.40	0.08	0.5385	0.0042	1.0395	0.0043
PM1-2821	PM-1	2820.5	Interior Intact	40690	3.67	0.01	26.85	0.11	1.0357	0.0063	1.0513	0.0023
PM1-3141	PM-1	3140.5	Interior Intact	40690	1.18	0.01	18.85	0.07	1.0097	0.0071	1.0112	0.0027
PM1-3456	PM-1	3456.4	Interior Intact	40695	3.68	0.01	20.74	0.14	0.9720	0.0071	0.9959	0.0044
PM1-5598	PM-1	5597.5	Discrete Fracture	40708	8.72	0.03	25.22	0.19	0.9594	0.0055	0.9968	0.0029
PM1-5780	PM-1	5779.6	Discrete Fracture	40708	2.88	0.01	16.31	0.10	1.2348	0.0116	1.2393	0.0037
PM1-5997	PM-1	5996.5	Discrete Fracture	40708	4.72	0.02	26.64	0.21	1.7393	0.0181	1.7763	0.0049
PM1-6084	PM-1	6084	Discrete Fracture	40708	4.39	0.01	33.24	0.28	1.3863	0.0145	1.3662	0.0037
PM1-6079	PM-1	6079	Brecciated/Rubblized	40695	5.48	0.02	27.73	0.15	0.9640	0.0061	1.0056	0.0029
PM1-6614	PM-1	6614	Interior Intact	40695	4.28	0.01	24.18	0.13	0.9185	0.0053	0.9668	0.0061
UE19fs-2554 ()	UE-19fs	2554	Discrete Fracture	40725	43.79	0.14	15.79	0.09	0.8604	0.0044	0.9744	0.0026
UE19fs-3375 ()	UE-19fs	3375	Discrete Fracture	40725	2.80	0.01	6.73	0.04	0.4487	0.0052	0.9909	0.0031
UE19fs-3552 ()	UE-19fs	3552	Discrete Fracture	40726	2.86	0.01	5.54	0.03	0.2850	0.0088	1.0175	0.0032
UE19fs-4303 ()	UE-19fs	4303	Discrete Fracture	40725	4.17	0.01	3.83	0.02	0.4203	0.0060	1.2344	0.0034
UE19fs-4913 ()	UE-19fs	4913	Discrete Fracture	40726	1.13	0.01					1.0168	0.0029
UE19fs-5211 ()	UE-19fs	5211	Discrete Fracture	40726	7.98	0.03	10.93	0.06	0.1914	0.0016	2.0915	0.0056
UE19fs-5517	UE-19fs	5516.6	Brecciated/Rubblized	40697	6.03	0.02	25.58	0.20	0.9874	0.0055	0.9934	0.0025
UE19fs-5517 ()	UE-19fs	5517	Discrete Fracture	40726	11.02	0.03	30.95	0.25	0.9720	0.0056	0.9890	0.0026
UE19gs-2136	UE-19gs	2136	Brecciated/Rubblized	40690	1.06	0.01					0.9980	0.0041
UE19gs-2136 ()	UE-19gs	2136	Discrete Fracture	40727	0.43	0.01	1.17	0.01	1.2635	0.0393	1.4265	0.0607
UE19gs-4054	UE-19gs	4054	Brecciated/Rubblized	40696	7.97	0.03					0.9986	0.0027
UE19gs-4658	UE-19gs	4657.5	Discrete Fracture	40696	3.40	0.01	15.99	0.09	1.0013	0.0066	1.0316	0.0029
UE19gs-4658 ()	UE-19gs	4658	Discrete Fracture	40726	9.37	0.03	14.85	0.08	1.3603	0.0080	1.6258	0.0045
UE19gs-4814	UE-19gs	4814.3	Interior Intact	40696	2.95	0.01	15.59	0.11	0.9920	0.0059	1.0044	0.0033
UE19gs-4908	UE-19gs	4907.8	Discrete Fracture	40696	2.37	0.01					0.9984	0.0026
UE19gs-5303 ()	UE-19gs	5303	Discrete Fracture	40726	7.42	0.02	19.23	0.13	1.0721	0.0098	1.1220	0.0029
UE19gs-5641 ()	UE-19gs	5641	Discrete Fracture	40726	2.31	0.01	5.63	0.03	1.2653	0.0128	1.3724	0.0056
UE19gs-5816	UE-19gs	5815.6	Brecciated/Rubblized	40697	4.25	0.01					1.0133	0.0027
UE19gs-6279 ()	UE-19gs	6279	Brecciated/Rubblized	40696	3.97	0.01	23.42	0.12	0.9852	0.0315	1.0260	0.0030
UE19gs-6279 ()	UE-19gs	6279	Discrete Fracture	40726	3.96	0.01	22.65	0.16	1.1478	0.0056	1.1805	0.0034
UE19i-2419	UE-19i	2419	Interior Intact	40697	4.61	0.01	23.28	0.21	1.0655	0.0464	1.0536	0.0028
UE19i-2891 ()	UE-19i	2891	Discrete Fracture	40727	19.07	0.06					1.3924	0.0037

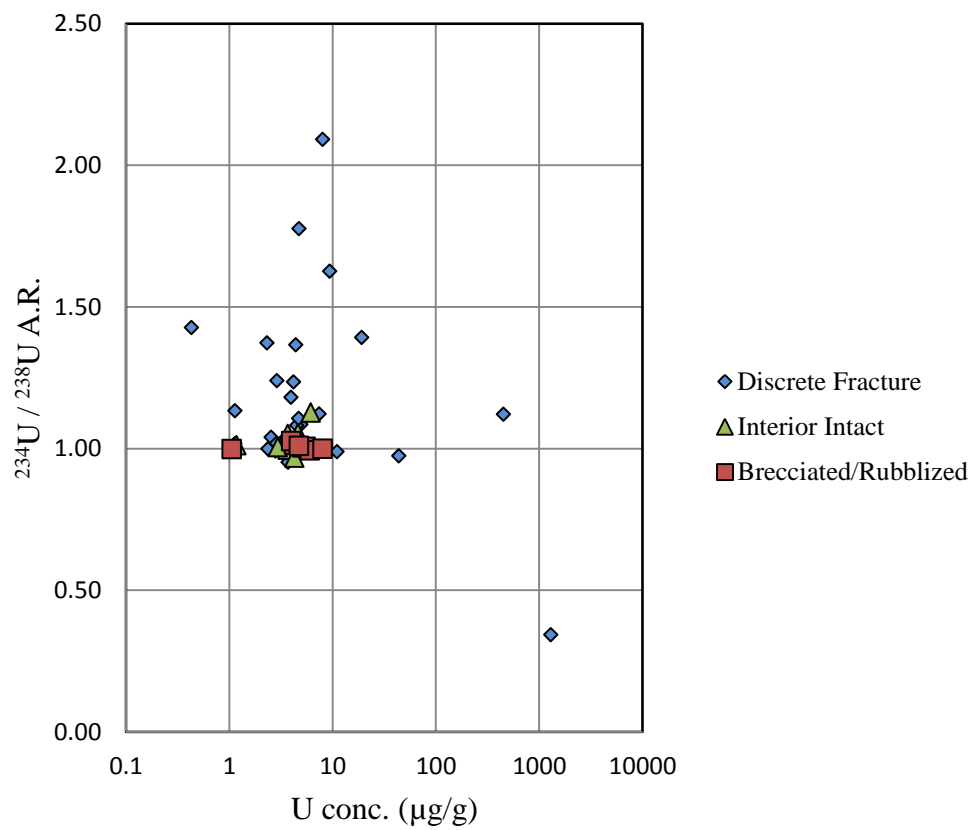| UE19i-3533 ()	UE-19i	3533	Discrete Fracture	40727	4.92	0.02	14.20	0.09	1.0871	0.0070	1.0848	0.0028
UE20f-2845	UE-20f	2845.4	Discrete Fracture	40707	450.34	1.60	31.37	0.19	0.7820	0.0045	1.1211	0.0029
UE20f-2849	UE-20f	2849	Discrete Fracture	40708	1294.16	5.60	55.10	0.47	0.3802	0.0023	0.3421	0.0009
UE20f-3030 ()	UE-20f	3030	Discrete Fracture	40725	4.48	0.01	12.26	0.08	0.6697	0.0084	1.0812	0.0028
UE20f-3030	UE-20f	3030.4	Brecciated/Rubblized	40696	4.72	0.02	23.48	0.15	0.9751	0.0060	1.0094	0.0028
UE20f-3607 ()	UE-20f	3607	Discrete Fracture	40725	5.04	0.02					0.9960	0.0044
UE20f-3704	UE-20f	3704.4	Discrete Fracture	40708	4.68	0.02	3.90	0.02	0.9906	0.0058	1.1067	0.0030
UE20f-3904	UE-20f	3904.2	Interior Intact	40695	5.07	0.02	18.74	0.10	0.9979	0.0064	1.0031	0.0027
UE20f-4160	UE-20f	4159.8	Interior Intact	40696	6.14	0.02	19.37	0.18	1.1261	0.0330	1.1270	0.0031
UE20f-4741	UE-20f	4740.7	Discrete Fracture	40708	1.13	0.01	6.23	0.04	1.0673	0.0113	1.1332	0.0038
UE20f-5291	UE-20f	5290.7	Discrete Fracture	40708	3.72	0.01	14.33	0.17	0.9576	0.0070	0.9516	0.0030
PM1-2366 ()	PM-1	2366	Discrete Fracture	40725	2.54	0.01	10.41	0.08	0.5385	0.0042	1.0395	0.0043
PM1-2821	PM-1	2820.5	Interior Intact	40690	3.67	0.01	26.85	0.11	1.0357	0.0063	1.0513	0.0030
PM1-3141	PM-1	3140.5	Interior Intact	40690	1.18	0.01	18.85	0.07	1.0097	0.0071	1.0117	0.0027
PM1-3456	PM-1	3456.4	Interior Intact	40695	3.68	0.01	20.74	0.14	0.9720	0.0071	0.9959	0.0044
PM1-5598	PM-1	5597.5	Discrete Fracture	40708	8.72	0.03	25.22	0.17	0.9594	0.0055	0.9968	0.0029
PM1-5780	PM-1	5779.6	Discrete Fracture	40708	2.88	0.01	16.31	0.10	1.2348	0.0116	1.2393	0.0037
PM1-5997	PM-1	5996.5	Discrete Fracture	40708	4.72	0.02	26.64	0.21	1.7393	0.0181	1.7763	0.0049
PM1-6084	PM-1	6084	Discrete Fracture	40708	4.39	0.01	33.24	0.28	1.3863	0.0145	1.3662	0.0037
PM1-6079	PM-1	6079	Brecciated/Rubblized	40695	5.48	0.02	27.73	0.15	0.9640	0.0061	1.0056	0.0029
PM1-6614	PM-1	6614	Interior Intact	40695	4.28	0.01	24.18	0.13	0.9185	0.0053	0.9668	0.0061

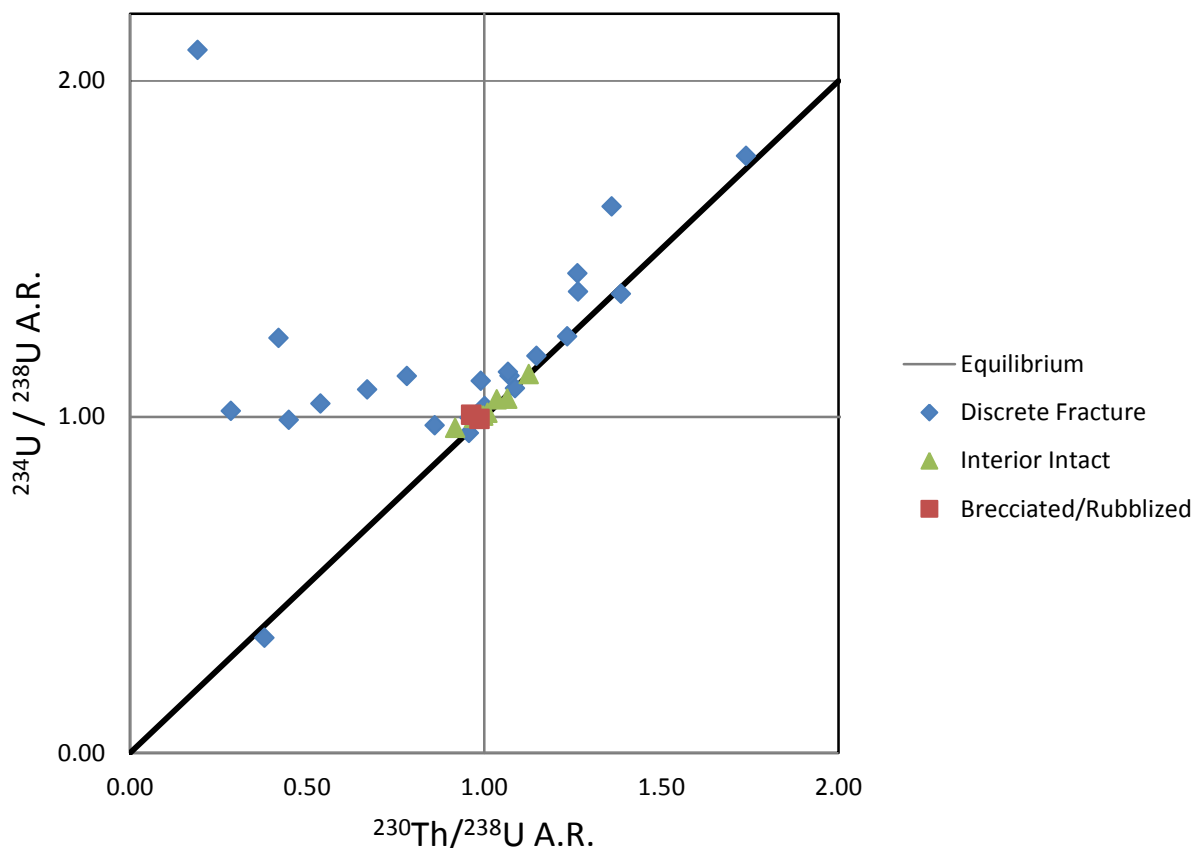**Figure 5-1. Relation of ^{234}U/^{238}U A.R. with total U concentration**

Figure 5-2. Samples' relationships to the ^{234}U/^{230}Th "Equiline"

Analytical results for 53 whole rock samples from Pahute Mesa are given in Table 5-1

and depicted graphically in Figures 5-1 and 5-2. In this sampling, there were 33 analyses of

discrete fracture surfaces, 12 analyses of interior intact rock samples, and 8 analyses of

brecciated/rubblized whole rock. Of the 33 discrete fractures analyzed, 24 have ^{234}U/^{238}U A.R.s

that differ from secular equilibrium (^{234}U/^{238}U A.R.=^{230}Th/^{238}U A.R.) by more than 2%. The

majority of discrete fracture surfaces are enriched in ^{234}U; that is, having ^{234}U/^{238}U A.R.s greater

than 1.02. This demonstrates that the majority of fracture surfaces selected in this study show

evidence for significant water-matrix rock interaction over the last 500,000 years (Latham and

Schwarcz, 1987). Specifically, these results show that ^{234}U tends to be preferentially deposited

on discrete fracture surfaces relative to ^{238}U. This is consistent with ^{234}U/^{238}U A.R.s between 2

and 6 measured for groundwaters from in nearby wells (Paces et al., 2002).

In contrast, only 7 out of the 20 total interior intact and brecciated/rubblized samples

show ^{234}U/^{238}U A.R.s that differ from secular equilibrium by more than ±2%. This suggests little

water-rock interaction over the last 500,000 years. The distribution U-series isotopic

compositions with respect to secular equilibrium values are displayed in Figure 5-2. Box-and-

whisker plots (Figure 5-3) show the distribution of ^{234}U/^{238}U A.Rs classified into three different

sample groupings. The blue boxed regions represent the 25% to 75% quartile range with black

lines extending to extreme data points not classified as outliers, the red line represents the

median value, and the red crosses represent data points that are considered outliers by MATLAB
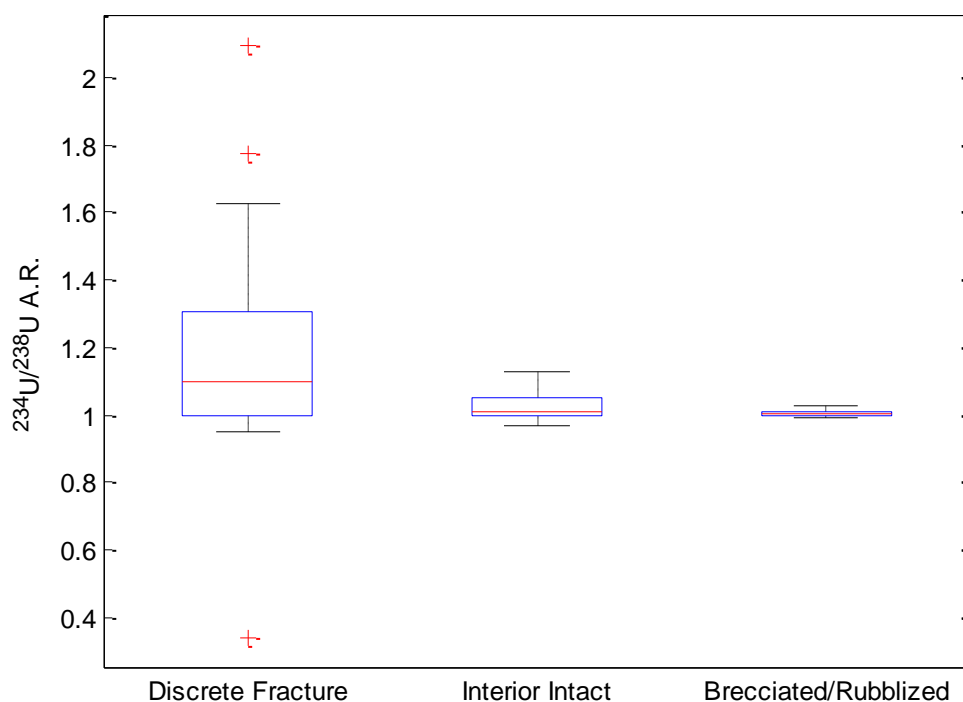
R2011b.

Figure 5-3. Box and Whisker Plot of the ^{234}U/^{238}U A.R.s for whole rock analyses

Plotting $^{234}U/^{238}U$ A.R. vs $^{230}Th/^{238}U$ A.R. (Figure 5-2) for all of the data samples

provides further insight into the ground water flow at Pahute Mesa. Many samples have

$^{230}Th/^{238}U$ A.R compositions similar to $^{234}U/^{238}U$ A.R.s and plot along the so-called "equiline" -

defined as $^{234}U/^{238}U$ A.R. equals $^{230}Th/^{238}U$ A.R. This relation is not expected for closed-system

isotope evolution of fracture minerals precipitated from groundwater with initial compositions of

$^{234}U/^{238}U$ A.R. >1.0 and $^{230}Th/^{238}U$ A.R.=0.0. Nevertheless, the systematic distribution of data

along and to the left of the equiline is not likely to be coincidental.

U-series compositions plotting along the equiline have been interpreted as the result of

steady state long-term balance between contrasting processes involving sorption, leaching, and

radioactive decay (Dequincey et al., 2002). This is further investigated in Chapter 6 of this

report. The fact that most samples, especially discrete fracture surfaces, display substantial

amounts of isotopic disequilibrium ($^{234}U/^{238}U$ and $^{230}Th/^{238}U$ A.R.s not equal to 1.0) indicates

continual or recently episodic water-matrix interaction. The fact that samples of bulk matrix

material (brecciated/rubblized and interior intact core types) have $^{234}U/^{238}U$ and $^{230}Th/^{238}U$ A.R.s

that are much closer to 1.0 compared to discrete fracture samples is consistent with flow being

dominated by secondary permeability.

Many of the discrete fracture surface samples plot to the left of the equiline with

$^{234}U/^{238}U$ A.R. values that are consistent with fracture surfaces interacting with solutions that had

elevated $^{234}U/^{238}U$ A.R.s in the recent past. However, many of these samples have measured

$^{234}U/^{238}U$ A.R. values that are substantially lower (~0.98 to 1.20) than those typically observed in

groundwater from the surrounding area (2 to 6). These compositions are difficult to explain by

the simple precipitation of young secondary minerals to fracture surfaces followed by closed

system isotope evolution. Furthermore, very few samples have ^{234}U/^{238}U A.R. values that are less than 1.0, which is typically attributed to the effects of preferential removal of ^{234}U by leaching processes (Latham and Schwarcz, 1987). The clear exception is a single sample of a discrete fracture surface from borehole UE-20f (UE20f-2849) that has an extremely depleted ^{234}U/^{238}U A.R. value of ~0.34. Despite this very low value, the ^{230}Th/^{238}U A.R. for this same sample is similar (~0.38) and like other samples with ^{234}U/^{238}U A.R. values > 1.0, data from UE20f-2849 also plots along the equiline. It is notable that data plotting to the right of equiline, indicative of ^{230}Th/^{238}U A.R. > ^{234}U/^{238}U A.R., are essentially absent despite the wide range of observed disequilibrium values. This distribution of U-series data is unlike that reported for a number of other studies of U-series isotopes in environments involving water-rock interaction that commonly show solids with ^{230}Th/^{238}U A.R. > ^{234}U/^{238}U A.R. (Latham and Schwarcz, 1987; Dequincy et al., 2002; Paces et al., 2006; Thiel et al., 1983). The strong evidence of fracture dominated groundwater flow at Pahute Mesa led us to further investigate water-matrix interaction by exploring ^{234}U/^{238}U and ^{230}Th/^{234}U in the rock matrix with distance away from discrete fracture surfaces.

Whole Rock Wafer Analysis

A total of four wafer profiles from Pahute Mesa were selected in order to preform U-series analysis at distances perpendicular to the fracture surfaces. The four fracture surfaces targeted for wafer analysis were selected for their high degree of secular disequilibrium. They are as follows: UE19fs-5211', UE19gs-4658', UE20f-2849', and PM1-6084'.

In order to perform the wafer analysis for each of the four selected samples, a core was drilled perpendicularily from the previously scaped fracture surface. This sampling procedure for the PM1-6084' discrete fracture surface sample can be seen in the photographs given in Figure 5-4 below.
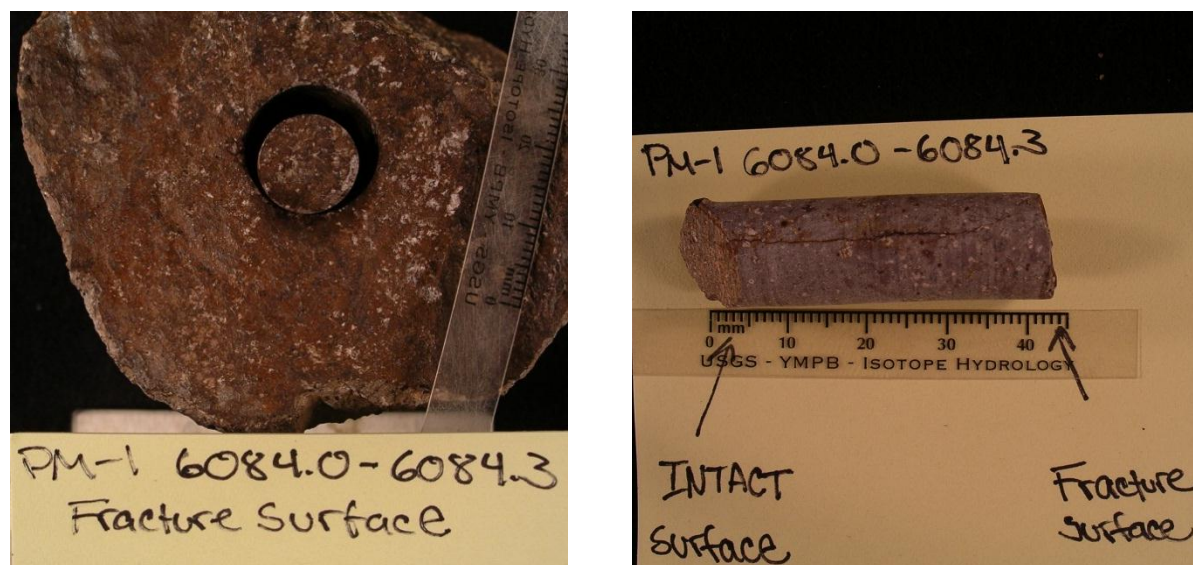
Figure 5-4. Sampling procedure for wafer analysis.

This process was performed using a 0.25 inch-diameter drill core bit. The resulting 15 to 44 mm long cores were then cut into wafers parallel to the fracture surface as a means of obtaining subsamples spaced evenly away from the fracture surface into the rock matrix. Significant effort was made to ensure equal thickness among the wafers. Wafers representing rock matrix at known distances away from the fracture surface were then ground to a fine powder using an agate mortar and pestle, chemically digested, and analyzed for U-series isotopes in the same manner as previously described. Table 5-2 gives approximate wafer distance intervals for the four cores.

Table 5-2. Cutting Specifications of Core for Wafer Analysis

Sample name	Core length (mm)	No. of Samples	Average distance interval (mm)
UE19fs-5211	15	6	2.5
UE19gs-4658	42	17	2.5
UE20f-2849	24	12	2.0
PM1-6084	44	18	2.4

In addition to U-series isotope measurements, estimates of porosity were made using petrographic examinations. In order to perform these measurements, a second 0.25 inch-diameter core was drilled through the discrete fracture samples adjacent to the first core, but in an area where the fracture surface coating was not removed. This core was then cut longitudinally, impregnated with blue epoxy, and made into a 30 μm thick thin section. A binary averaging procedure was used in Reindeer Graphics Add-in to Abode Photoshop in order to quantify the relative pore space in the each of the thin sections. In this procedure, 3 photomicrographic images were taken of each thin section. Each digital image covered an area approximately 3.3 mm x 2.5 mm and contained a total pixel count of 3,145,728. Imaging software then counted the number of pixels representing blue-stained epoxy. This process was done twice for each image. This method of porosity measurement is similar to the method described in detail by Sak et al. (2010), which used ImageJ processing software to arrive at porosity measurements.

In addition, porosity measurements were made by standard point counting methods while viewing thin sections under a petrographic microscope. A mechanical stage was used to provide a rectilinear grid with ~1 mm x 1 mm point spacing. A total of 1,000 counts were made for each thin section sample where each point was classified either as "void", corresponding to pore

space, or "solid", corresponding to rock crystal. Porosity measurements for UE19fs-5211,

UE19gs-4658, UE20f-2849, and PM1-6084 can be seen in Table 5-3.

Table 5-3. Porosity Measurements for selected wafer profiles

Borehole ID	Porosity (%)	
	Photoshop	Point Count
Ue19fs-5211	6.9	27.3
UE19gs-4658	3	9.8
UE20f-2849	1.6	5.3
PM1-6084	2.2	10.6

As seen in Table 5-3 above, the two different porosity measurement techniques explored

in this thesis yield very different results. It is likely that the point counting method produces the

most accurate representation of the pore space in the rock matrix, since its measurements are not

dependent on color spectrum interpretations as in Photoshop but, instead rely on visual

evaluation of each of the 1,000 point classifications per sample.

Table 5-4 and Figures 5-5 to 5-8 summarize the results of the wafer profile analysis.

Samples were named in a manner that allowed for the illustration of what wafer number they

corresponded to out of the total number of wafers for that samples, with the smaller wafer

numbers being closer to the discrete fracture surface. For example UE19fs-5211_1/6 corresponds

to the first of 6 total wafers that were made for UE19fs-5211'. UE19fs-5211_0 corresponds to

the discrete fracture surface itself. The accompanying qualitative interpretations are suggested

explanations for the complicated nature of the water-rock interaction at Pahute Mesa, which is

likely governed by different water and rock compositions in different areas as well as differences

in groundwater advection rates and time-dependent chemical and mineralogical properties of

fracture surfaces. Unfortunately, Th isotope data is not available for sample UE19gs-4658_1/17

due to an experimental mishap. Furthermore, it is noted that subsamples represent a mixture of

all materials within the finite volume and may reflect mixtures of individual layers (i.e.,

secondary mineral coating and underlying host rock) that could not be sampled as separate and

discrete layers.

Table 5-4. Wafer sample U-series results

Sample Name	Borehole	Profile sequence	Distance from fracture surface (mm)	Sample Type	Analysis Date	U concen-tration, in ppm	±2s	Th concen-tration, in ppm	±2s	230Th/238U AR	±2s	234U/238U AR	±2s
UE19fs-5211_0	UE-19fs			Discrete Fracture	40726	7.98	0.03	10.93	0.06	0.1914	0.0016	2.0915	0.0056
UE19fs-5211_1/6	UE-19fs	1	2.5	Wafer Profile	40803	14.19	0.04	23.23	0.16	0.9240	0.0047	0.9474	0.0023
UE19fs-5211_2/6	UE-19fs	2	5.0	Wafer Profile	40772	14.26	0.05	24.73	0.22	0.8876	0.0050	0.9075	0.0024
UE19fs-5211_3/6	UE-19fs	3	7.5	Wafer Profile	40772	12.48	0.04	25.32	0.23	0.9198	0.0053	0.9383	0.0026
UE19fs-5211_4/6	UE-19fs	4	10.0	Wafer Profile	40772	11.83	0.04	24.94	0.20	0.9257	0.0051	0.9496	0.0026
UE19fs-5211_5/6	UE-19fs	5	12.5	Wafer Profile	40772	11.24	0.04	27.01	0.22	0.9432	0.0066	0.9627	0.0027
UE19fs-5211_6/6	UE-19fs	6	15.0	Wafer Profile	40773	13.20	0.04	30.37	0.19	0.9528	0.0053	0.9604	0.0025
UE19gs-4658_0	UE-19gs			Discrete Fracture	40726	9.37	0.03	14.85	0.08	1.3603	0.0080	1.6258	0.0045
UE19gs-4658_1/17	UE-19gs	1	2.5	Wafer Profile	40803	3.40	0.01		0.08			1.0410	0.0040
UE19gs-4658_2/17	UE-19gs	2	4.9	Wafer Profile	40838	3.13	0.01	15.64	0.08	0.9915	0.0083	1.0110	0.0034
UE19gs-4658_3/17	UE-19gs	3	7.4	Wafer Profile	40804	5.91	0.10	14.66	0.08	0.5406	0.0173	1.1217	0.0092
UE19gs-4658_5/17	UE-19gs	5	12.4	Wafer Profile	40838	4.01	0.01	16.59	0.09	0.9925	0.0115	1.0027	0.0030
UE19gs-4658_8/17	UE-19gs	8	19.8	Wafer Profile	40804	3.43	0.01	16.92	0.09	0.9516	0.0544	1.0055	0.0026
UE19gs-4658_11/17	UE-19gs	11	27.2	Wafer Profile	40838	3.19	0.010	17.48	0.10	0.9981	0.0112	1.0032	0.0029
UE20f-2849_0	UE-20f			Discrete Fracture	40708	1294.17	5.60	55.10	0.47	0.380184	0.0023	0.3421	0.0009
UE20f-2849_1/12	UE-20f	1	2.0	Wafer Profile	40804	80.52	0.63	16.59	0.09	0.457232	0.0041	0.4227	0.0012
UE20f-2849_2/12	UE-20f	2	4.0	Wafer Profile	40838	2.69	0.01	14.66	0.12	1.363599	0.0102	1.0747	0.0035
UE20f-2849_3/12	UE-20f	3	6.0	Wafer Profile	40804	3.14	0.01	19.68	0.14	1.242921	0.0117	1.0084	0.0047
UE20f-2849_5/12	UE-20f	5	10.0	Wafer Profile	40840	2.82	0.01	16.44	0.11	1.396746	0.0091	1.0668	0.0040
UE20f-2849_6/12	UE-20f	6	12.0	Wafer Profile	40804	2.87	0.01	16.60	0.13	1.414609	0.0109	1.0612	0.0028
UE20f-2849_8/12	UE-20f	8	16.0	Wafer Profile	40804	2.76	0.01	15.59	0.14	1.462378	0.0168	1.0617	0.0030
PM1-6084_0	PM-1			Discrete Fracture	40708	4.39	0.01	33.25	0.28	1.386282	0.0145	1.3662	0.0037
PM1-6084_1/18	PM-1	1	2.4	Wafer Profile	40803	6.46	0.02	33.15	0.31	0.951372	0.0131	0.9862	0.0027
PM1-6084_2/18	PM-1	2	4.9	Wafer Profile	40772	5.49	0.02	29.17	0.23	1.008377	0.0060	0.9969	0.0026
PM1-6084_4/18	PM-1	4	9.8	Wafer Profile	40772	5.63	0.02	28.98	0.36	0.995056	0.0056	1.0006	0.0026
PM1-6084_9/18	PM-1	9	22.0	Wafer Profile	40772	5.55	0.02	30.12	0.24	0.991133	0.0061	0.9996	0.0026
PM1-6084_16/18	PM-1	16	39.1	Wafer Profile	40772	5.33	0.023	34.05	0.32	0.999766	0.0060	1.0015	0.0028

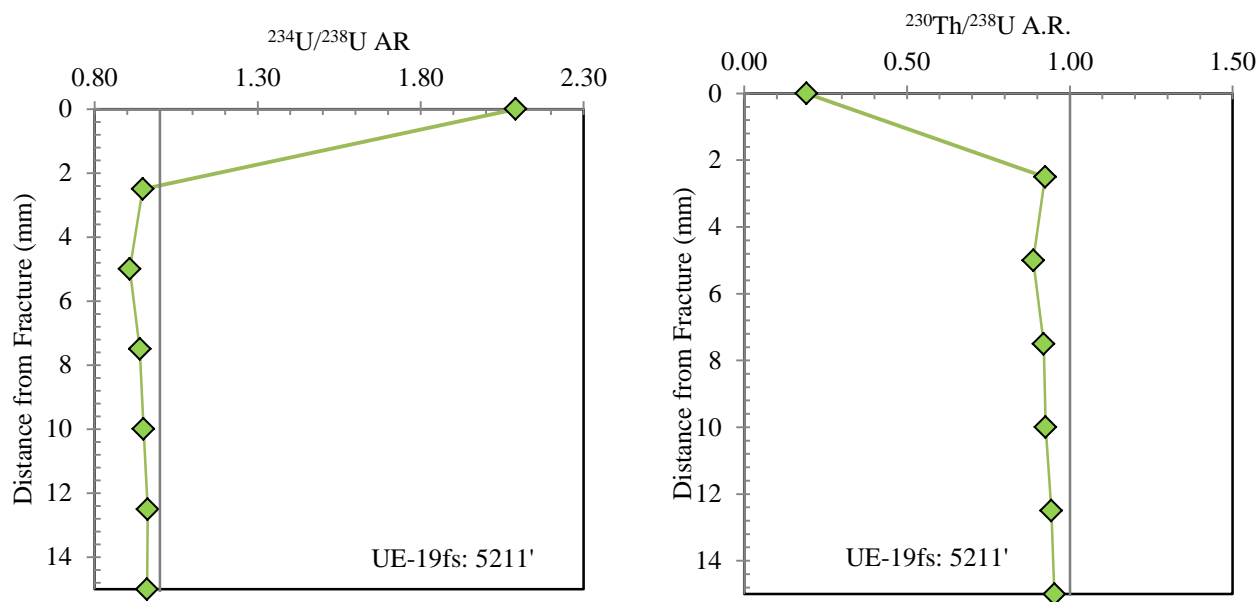**Figure 5-5. Profiles of ^{234}U/^{238}U A.R. and ^{230}Th/^{238}U A.R. variation with distance from fracture surface for wafers sampled from UE-19fs:5211'**

Seen in Figure 5-5, the presence of a relatively high ^{234}U/^{238}U A.R. and low ^{230}Th/^{238}U A.R. for the discrete fracture surface from sample UE-19fs:5211' (2.09 and 0.19, respectively) is consistent with the presence of recently deposited minerals on the fracture surface. This explains the relatively low ^{230}Th/^{238}U A.R. and the large difference in U-series isotope ratios (i.e., ^{234}U/^{238}U A.R. >> ^{230}Th/^{238}U A.R.). U-series compositions of subjacent samples are notably different from those of the fracture surface. Wafer samples have similar U-series isotope ratios and plot along the equiline at values between 0.90 and 0.96. This suggests that the rock matrix is much less susceptible to water-rock interaction than fracture minerals, but that pore water was still able to imbibe into the host rock. Since ^{234}U/^{238}U A.R.s are less than 1.0, the system is dominated by a loss of ^{234}U (which is preferentially leached compared to ^{238}U). Furthermore, the two wafers closest to the fracture surface have greater amounts of disequilibrium (lower ^{234}U/^{238}U A.R. and ^{230}Th/^{238}U A.R. values) than wafers at greater distances. The relatively large amount of disequilibrium observed in the rock matrix part of this profile is consistent with the

higher porosities measured in this sample (Table 5-3). The presence of greater disequilibrium in

wafers closer to the fracture surface is consistent with somewhat larger interactions near the
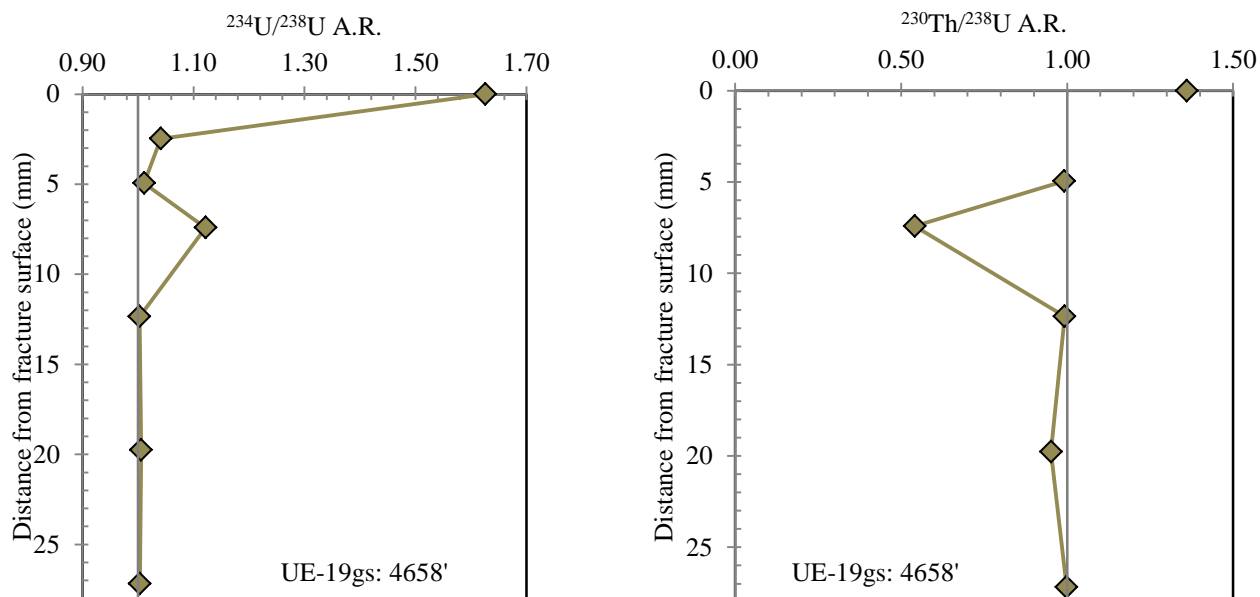
water/rock interface.

Figure 5-6. Profiles of ^{234}U/^{238}U AR and ^{230}Th/^{238}U AR variation with distance from fracture surface for wafers sampled from UE-19gs:4658'

Like the previous sample, the ^{234}U/^{238}U A.R. of the UE-19gs:4658' fracture surface is

elevated (1.63) indicating water-rock interaction. However, as seen in Figure 5-6, its ^{230}Th/^{238}U

A.R. is also relatively large (1.36) resulting in a composition that plots close to, but not on, the

equiline. This situation could be caused by the addition of secondary minerals precipitated from

groundwater solutions at some time in the past (more than 100,000 years ago), or by other

transient processes involving U uptake, removal, and decay. Both ^{234}U/^{238}U A.R.s and ^{230}Th/^{238}U

A.R.s for wafers in the interior of the sample trend toward secular equilibrium values suggesting

smaller amounts of water-rock interaction compared to UE-19fs:5211', which is consistent with

its lower measured porosity values. However, the wafer located at ~7mm from the fracture

surface presents an exception to the rest of the rock matrix samples in this profile. Its substantially higher $^{234}U/^{238}U$ A.R. and lower $^{230}Th/^{238}U$ A.R. value suggests the presence of a transient water-rock interaction event at this location. While the reason for this is unclear, it is possible that this isolated event occurred due to the presence of a small localized fissure containing recently deposited secondary minerals. Similar materials are not present in the immediately overlying wafer or two underlying wafers as the A.R.s are very close to secular equilibrium values.
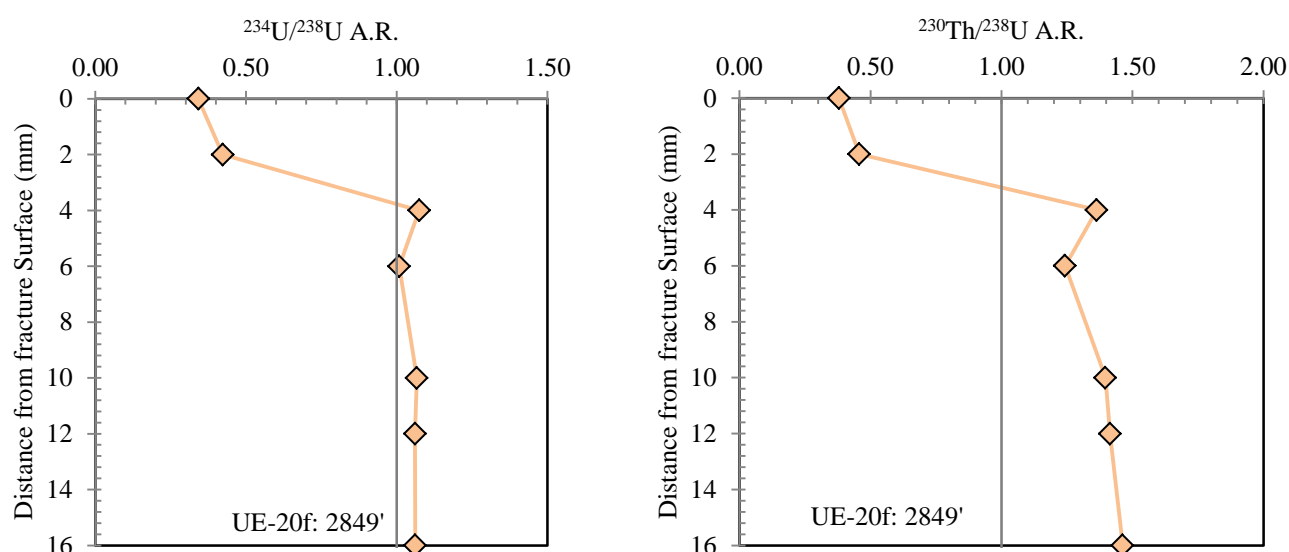

Figure 5-7. Profiles of $^{234}U/^{238}U$ AR and $^{230}Th/^{238}U$ AR variation with distance from fracture surface for wafers sampled from UE-20f:2849'

As demonstrated in Figure 5-7, the U-series isotopic compositions for the discrete fracture surface sample from UE-20f:2849'are very unique. The fracture surface's extremely low $^{234}U/^{238}U$ A.R. indicates a very high degree of preferential leaching of ^{234}U relative to ^{238}U. Nevertheless, the $^{230}Th/^{238}U$ A.R. is similar and the resulting $^{234}U/^{230}Th$ A.R. value of about 0.90 allows the data point to plot close to the equiline. These conditions can only be satisfied if large

amounts of U are added. This is consistent with the U concentration of 1294 ppm measured for the fracture material, which is about 2.5 orders of magnitude larger than the average U concentration measured in the rock matrix wafers (~2.9 ppm). The isotope results for the 1 mm thick layer of white secondary mineral forming the surface coating on this sample gives rise to the possibility that recoil processes are more important in governing the U-series behavior of the fracture surface relative to other samples; that is, ^{234}U is strongly removed from the fracture surface by actively flowing groundwater.

Wafers at greater distances away from the fracture surface also show U-series disequilibrium. The wafer subjacent to the layer of secondary fracture minerals has intermediate concentrations and isotope compositions between the outer surface and the matrix of the interior. Results for this layer likely represent a mechanical mixture of secondary mineral and rock matrix. Remaining wafers have more typical ^{234}U/^{238}U and ^{230}Th/^{238}U A.R. values ranging from 1.01 to 1.46 and suggest that water is able to penetrate into the rock matrix. However, the U-series isotope behavior in these samples is unique in that ^{230}Th/^{238}U A.R. values are higher than ^{234}U/^{238}U A.R. values. As a result, data plot to the right of the equiline with ^{234}U/^{230}Th A.R. values between 0.73 and 0.81. These materials represent the only rock samples analyzed in this study with evidence for removal of bulk U relative to Th in order to obtain ^{234}U/^{230}Th A.R. values significantly less than 1.0.
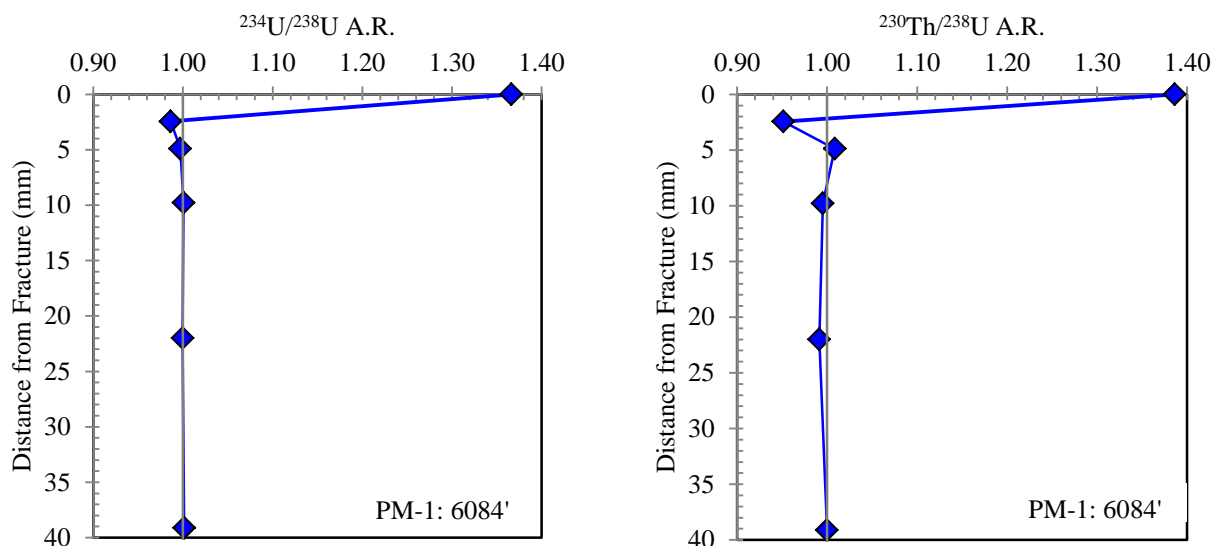
Figure 5-8. Profiles of ^{234}U/^{238}U AR and ^{230}Th/^{238}U AR variation with distance from fracture surface for wafers sampled from PM-1: 6084'

Results of isotope analysis for wafers from PM-1:6084' are shown in Figure 5-8. The fracture surface has elevated ^{234}U/^{238}U A.R. and ^{230}Th/^{238}U A.R. values that are nearly identical. The data for this point plots in close proximity to the equiline with a ^{234}U/^{230}Th A.R. value of 0.99. In contrast, wafers representing rock matrix at distance away from the fracture surface have U-series isotope ratios that are close to secular equilibrium values. The only significant exception is the first wafer at a distance of 2.4 mm which gives isotopic evidence of a relatively small amount ^{234}U leaching (^{234}U/^{238}U A.R. = 0.986) and addition of bulk U to explain the ^{230}Th/^{238}U A.R. of 0.951. ^{234}U/^{238}U A.R.s and ^{230}Th/^{238}U A.R.s for all other wafers are within 1% of the secular equilibrium values of 1.0. The fact that the compositions for the first wafer differ significantly from secular equilibrium suggests that water is capable of interacting with rock matrix within a few mm of the fracture surface, but that this point represents the extent of water-rock interaction in this particular rock despite porosities comparable to other rocks where more disequilibrium is observed.

CHAPTER 6

MODELING

Previous Approaches to Solving the Problem

A major focus of this study was to improve modeling techniques in order to better understand the movement of groundwater and its interaction with fracture networks in the saturated zone at Pahute Mesa. A numerical model that provides an explanation of the data set from Pahute Mesa has the potential to contribute to better predictions of future groundwater movement and the travel times and future locations of radioactive nuclides that were a result of underground detonations on the NNSS.

Latham and Schwarcz (1987) developed a model for characterizing U-concentrations in granite aquifers based on experimental leach rates of U, where leach rates were determined to be less than the decay rate of ^{230}Th. This model was developed assuming ^{230}Th is relatively immobile. Those authors also concluded that U-series nuclides could be considered to be in steady state secular equilibrium in deep subsurface zones, given the slow leach rates of U. This preferential leaching of ^{234}U relative to ^{238}U and U isotopes relative to ^{230}Th was further extended to models that considered both decay and leach rates, along with external fluxes of ^{238}U and ^{234}U nuclides (Dequincey et al., 2002). Porcelli et al. (2008) described in detail the chemical and physical exchange processes governing ^{238}U, ^{234}U, and ^{230}Th concentrations in flowing groundwater. Assuming that advection is the dominating physical process in the system (as opposed to dispersion), Porcelli et al. (2008) modified the traditional advection-dispersion equation to included nuclide source and sink terms. Source terms contributing ^{234}U to water

consist of weathering, alpha-recoil, desorption, and production, while sink terms removing U

from solution consist of precipitation, radioactive decay, and adsorption (Porcelli et. al 2008).

Aquifer rock-water interaction is largely based on alpha recoil and weathering rates, both of

which depend on the unique physical and chemical properties of the aquifer rock (Porcelli and

Swarzenski, 2003). These two studies did note however, that diffusion can play a dominant role

in nuclide concentration when considering locations inside of the bulk rock matrix at varying

distances away from the fracture surface. Moreover, these diffusive properties are very slow and

are characterized by transport through small pores in the matrix solid (Neretnieks, 1980).

Therefore, it was determined that diffusion would dominate advection when considering the

movement of groundwater through the matrix at distances away from the fracture surface.

Focusing on bulk adsorption and desorption rates, Krishnaswami et al. (1982) noted that

^{238}U, ^{234}U, and ^{230}Th can be added to groundwater by dissolution from the rock matrix,

radioactive decay of the parent nuclide, and alpha-recoil and desorption from the rock matrix

surface. This led to the development of a simple radionuclide transport model based on

first-order kinetic adsorption and desorption. It is of note that this model provides for nuclide

concentration via a balance between source and sink terms while ignoring both advective and

dispersive physical processes. This approach was subsequently used by Copenhaver et al. (1992)

in order to explain retardation factors in the transport of U-series nuclides. While considering

advective and dispersive processes, Maher et al. (2006) determined that alpha-recoil was largely

responsible for addition of radionuclides to actively flowing ground waters while dissolution and

decay governed the removal of radionuclides from ground water. Those authors also recognized

the importance of the rock surfaces' grain size distributions in determining the alpha–recoil

parameter. Similarly, Tricca et al. (2000) incorporated surface coating areas and densities, bulk

rock matrix densities, matrix water densities, and porosity in order to better characterize the radionuclide transport through groundwater.

A Diffusion-Based Approach to Modeling Wafer Profiles

In an attempt to explain the behavior of ^{234}U/^{238}U and ^{230}Th/^{238}U A.R.s at distances perpendicular to the fracture surface, a diffusion-based model was developed. This model was based on the previous approaches to characterize the interaction between aquifer material and actively flowing groundwater (Tricca et al., 2000; Porcelli and Swarzenski, 2003; Porcelli et al., 2008). Steady-state matrix water and matrix rock equations describing ^{238}U, ^{234}U, and ^{230}Th concentrations were developed as functions of perpendicular distance into the bulk rock material away from discrete fracture surfaces. Following Neretnieks (1980), diffusion was considered a governing process of nuclide transport in the matrix water. Governing equations for nuclide concentrations in the matrix rock did not include advection or diffusion due to the large time scales necessary for these processes to occur. Source and sink terms were represented using a simplified approach following Tricca et al. (2000) where bulk nuclide attachment and detachment terms and a recoil processes were assumed to govern the chemical behavior of U-series isotopes in the matrix rock and matrix water at distances away from the fracture surface. Boundary conditions were formulated to mimic groundwater U concentrations and ^{234}U/^{238}U A.R. values observed in samples of Pahute Mesa groundwater (Paces et al., 2002; J.B. Paces, USGS, unpublished data), and by assuming that at large distances away from the fracture surface, nuclide concentrations in the rock matrix were equal to those in the matrix water. That

is, at large distances from the fracture surface, ^{238}U, ^{234}U, and ^{230}Th concentrations in the rock matrix were set to be equal to those in the pore water.

This diffusion-based approach to modeling the U-series isotopic composition observed in wafer profiles in Figures 5-5 through 5-8 however did not prove to be fruitful. Using Wolfram Mathematica 8 and MATLAB R2011b to develop analytical and numerical solutions to nuclide concentrations, we were unable to match the ^{234}U/^{238}U A.R. and ^{230}Th/^{238}U A.R. curves shown in Figures 5-5 through 5-8. Attempts to match isotopic compositions heavily relied on varying values for bulk nuclide attachment and detachment terms. Based on the previously described model, simulations using nuclide concentrations measured at discrete fracture surfaces did not result in isotopic behavior observed in wafers away from the fracture surfaces as seen in Figures 5-5 through 5-8. Specifically, this model produced ^{234}U/^{238}U A.R.s that were much smaller than those observed in the wafer profiles.

The failure of our diffusion-based model to match the wafer profiles suggests that matrix rock and matrix water interaction is best characterized by a step function where the nuclide concentrations seen on the fracture surface are not directly related to the underlying rock matrix. Discrete fracture isotopic compositions are controlled by secondary mineral precipitates from advecting groundwaters that do not reflect the behavior of the interior of the rock. It is also possible that modeling matrix water and matrix rock interaction as a steady state process, with constant bulk attachment and detachment rates, is an inaccurate representation of the groundwater behavior at Pahute Mesa. The diffusion-based model in this thesis, only considered first order bulk attachments, leaving open the possibility for there to exist zero order and higher order processes that may greatly impact the behavior of radionuclides in discrete fracture networks. This leads to the conclusion that the physical and chemical processes at Pahute Mesa

are too unconstrained to obtain meaningful results from the diffusion model. Other studies

incorporated many complex constrained relationships to more completely characterize fracture

network flow in their models (Tricca et al., 2000; Maher et al., 2006). This included alpha-recoil

surface area relationship and fracture surface coating thickness and densities. Moreover, those

studies focused on modeling groundwater A.R.s as opposed to this study, which focused on

modeling rock A.R.s.

 Modeling Sample Locations Relative to the Equiline: Steady State Conditions

Due to the limited success of the diffusion-reaction models, we decided to pursue an

alternative approach that considers locally "well-mixed" behavior where the U-series isotopes

within fractures were constant throughout the fracture aperture. Specifically, we aim to explain

the location of the points on Figure 5-2 and their relationship secular equilibrium and to the

equiline. As noted by Dequincey et al. (2002), data points that fall on the equiline represent a

steady state balance between physical and chemical processes governing U-series nuclide

transport and decay. In order to constrain and quantitatively assess these processes, a steady state

numerical model similar to the approach taken by Dequincey et al. (2002) was developed. This

model considers a balance between inputs, decay, and outputs of radioactive ^{238}U, ^{234}U, and

^{230}Th, with decay constants of λ_{238}=1.55125E-10 yr^{-1}, λ_{234}=2.8262E-06 yr^{-1}, λ_{230}=9.158E-06 yr^{-1}

(Jaffey et al., 1971; Cheng et al., 2000). In order to simplify the model, it was assumed that ^{230}Th

was immobile; that is, it was not considered to be an input or output of the system. This

assumption is consistent with other equiline modeling approaches (Latham and Scwarcz, 1987;

Dequincey et al., 2002). Governing equations for the evolution of nuclide concentrations through time are given in Dequincey et al. (2002) for systems leading to steady-state ^{234}U /^{238}U and ^{230}Th /^{238}U A.R. compositions. The governing equations of U-series nuclide concentrations are given below:

$$\frac{d\,^{238}U}{dt} = \frac{F_{238}}{\lambda_{238}} - a_{238}\,^{238}U - \lambda_{238}\,^{238}U \tag{1}$$

$$\frac{d\,^{234}U}{dt} = \frac{F_{234}}{\lambda_{234}} + \lambda_{238}\,^{238}U - a_{234}\,^{234}U - \lambda_{234}\,^{234}U \tag{2}$$

$$\frac{d\,^{230}Th}{dt} = \lambda_{234}\,^{234}U - \lambda_{230}\,^{230}Th \tag{3}$$

where F_{234} and F_{238} are activity inputs (having units of $(g/g)/yr^2$) to the system and a_{238} and a_{234} are first-order rate constants (having units of yr^{-1}) for loss of ^{238}U and ^{234}U. The steady state solutions to these equations used to characterize samples with equivalent ^{234}U/^{238}U A.R.s and ^{230}Th/^{238}U A.R.s can be seen below:

$$\left(\frac{^{230}Th}{^{238}U}\right)_{SS} = \frac{\lambda_{234}(F_{234}/\lambda_{234})/(\lambda_{234}+a_{234})}{((F_{238}/\lambda_{238})/(\lambda_{238}+a_{238}))}\left(\frac{\lambda_{230}}{\lambda_{238}}\right) + \frac{\lambda_{230}}{\lambda_{234}+a_{234}} \tag{4}$$

$$\left(\frac{^{234}U}{^{238}U}\right)_{SS} = \frac{(F_{234}/\lambda_{234})/(\lambda_{234}+a_{234})}{((F_{238}/\lambda_{238})/(\lambda_{238}+a_{238}))}\left(\frac{\lambda_{234}}{\lambda_{238}}\right) + \frac{\lambda_{238}}{\lambda_{234}+a_{234}} \tag{5}$$

By examining the above equations, we can infer an "F-ratio" term, equal to the ratio of the input activity of ^{234}U divided by that of ^{238}U. The F-ratio term represents the total ^{234}U /^{238}U A.R. of the U-series nuclide source terms in the system. This leads to the development of equations 6 and 7.

$$\left(\frac{^{230}Th}{^{238}U}\right)_{SS} = \frac{\lambda_{234}(F_{Ratio}/\lambda_{234})/(\lambda_{234}+a_{234})}{((1/\lambda_{238})/(\lambda_{238}+a_{238}))}\left(\frac{\lambda_{230}}{\lambda_{238}}\right) + \frac{\lambda_{230}}{\lambda_{234}+a_{234}} \tag{6}$$

$$\left(\frac{^{234}U}{^{238}U}\right)_{SS} = \frac{(F_{Ratio}/\lambda_{234})/(\lambda_{234}+a_{234})}{((1/\lambda_{238})/(\lambda_{238}+a_{238}))}\left(\frac{\lambda_{234}}{\lambda_{238}}\right) + \frac{\lambda_{238}}{\lambda_{234}+a_{234}} \qquad \text{(7)}$$

This term, along with an "a-ratio" term that is equal to the ratio of the loss rate constant of ^{234}U divided by ^{238}U allowed for further characterization of points along the equiline. Steady state a-ratios were found by matching observed and modeled A.R.s for all samples analyzed from Pahute Mesa. This analysis was based on F-ratio values consistent with the ^{234}U /^{238}U A.R. assumed for the nearest available groundwater based on data from wells on Pahute Mesa (J.B. Paces, USGS, unpublished data). Results are presented in Table 6-1 on the following page and can be further visualized in the following two figures. In the Figures 6-1 and 6-2, the values adjacent to the data points represent the a-ratio values and the equiline is represented by a solid red line.

Table 6-1. Steady State a_{234} and a_{238} values for samples with ^{234}U/^{230}Th A.R. values ranging from 0.85 to 1.15

| Sample	Treatment	^{230}Th/^{238}U A.R.	^{234}U/^{238}U A.R.	F-ratio	a_{238} (yr^{-1})	a_{234} (yr^{-1})	a_{234}/a_{238}
PM-1:2821	Interior Intact	1.0357	1.0513	4.3	1.6300E-06	6.5565E-06	4.0
PM-1:3141	Interior Intact	1.0070	1.0117	4.3	1.6022E-06	6.7839E-06	4.2
PM-1:3456	Interior Intact	0.9720	0.9959	4.3	1.6502E-06	7.1356E-06	4.3
PM-1:5598	Discrete Fracture	0.9594	0.9968	4.3	1.6811E-06	7.2595E-06	4.3
PM-1:5780	Discrete Fracture	1.2348	1.2393	4.3	1.6058E-06	5.1307E-06	3.2
PM-1:5997	Discrete Fracture	1.7392	1.7763	4.3	1.6432E-06	2.9792E-06	1.8
PM-1:6079	Brecciated/Rubblized	0.9640	1.0056	4.3	1.6900E-06	7.2139E-06	4.3
PM-1:6084	Fracture (wafer)	1.3863	1.3662	4.3	1.5671E-06	4.3200E-06	2.8
PM-1:6614	Interior Intact	0.9185	0.9668	4.3	1.7098E-06	7.6844E-06	4.5
UE-19fs:2554	Discrete Fracture	0.8605	0.9744	1.5	5.3891E-06	8.3568E-06	1.6
UE-19fs:5517	Discrete Fracture	0.9720	0.9890	1.5	4.6881E-06	7.1358E-06	1.5
UE-19fs:5517	Brecciated/Rubblized	0.9874	0.9934	1.5	4.6179E-06	6.9883E-06	1.5
UE-19gs:4814	Interior Intact	0.9920	1.0044	6.7	1.0426E-06	6.9460E-06	6.7
UE-19gs:5303	Discrete Fracture	1.0721	1.1220	6.7	1.0891E-06	6.2561E-06	5.7
UE-19gs:5641	Discrete Fracture	1.2653	1.3723	6.7	1.1410E-06	4.9517E-06	4.3
UE-19gs:6279	Discrete Fracture	1.1478	1.1805	6.7	1.0645E-06	5.6926E-06	5.3
UE-19gs:6279	Brecciated/Rubblized	0.9852	1.0260	6.7	1.0820E-06	7.0091E-06	6.5
UE-19i:2419	Interior Intact	1.0655	1.0536	1.5	4.5125E-06	6.3087E-06	1.4
UE-19i:3533	Discrete Fracture	1.0871	1.0848	1.5	4.5679E-06	6.1381E-06	1.3
UE-20f:2849	Fracture (wafer)	0.3802	0.3421	2.7	2.2052E-06	2.1802E-05	9.9
UE-20f:3030	Brecciated/Rubblized	0.9751	1.0094	2.7	2.6642E-06	7.1057E-06	2.7
UE-20f:3704	Discrete Fracture	0.9906	1.1067	2.7	2.9425E-06	6.9587E-06	2.4
UE-20f:3904	Interior Intact	0.9979	1.0031	2.7	2.5626E-06	6.8909E-06	2.7
UE-20f:4160	Interior Intact	1.1261	1.1270	2.7	2.5477E-06	5.8462E-06	2.3
UE-20f:4741	Discrete Fracture	1.0673	1.1332	2.7	2.7544E-06	6.2947E-06	2.3
UE-20f:5291	Discrete Fracture	0.9576	0.9516	2.7	2.5236E-06	7.2777E-06	2.9

44
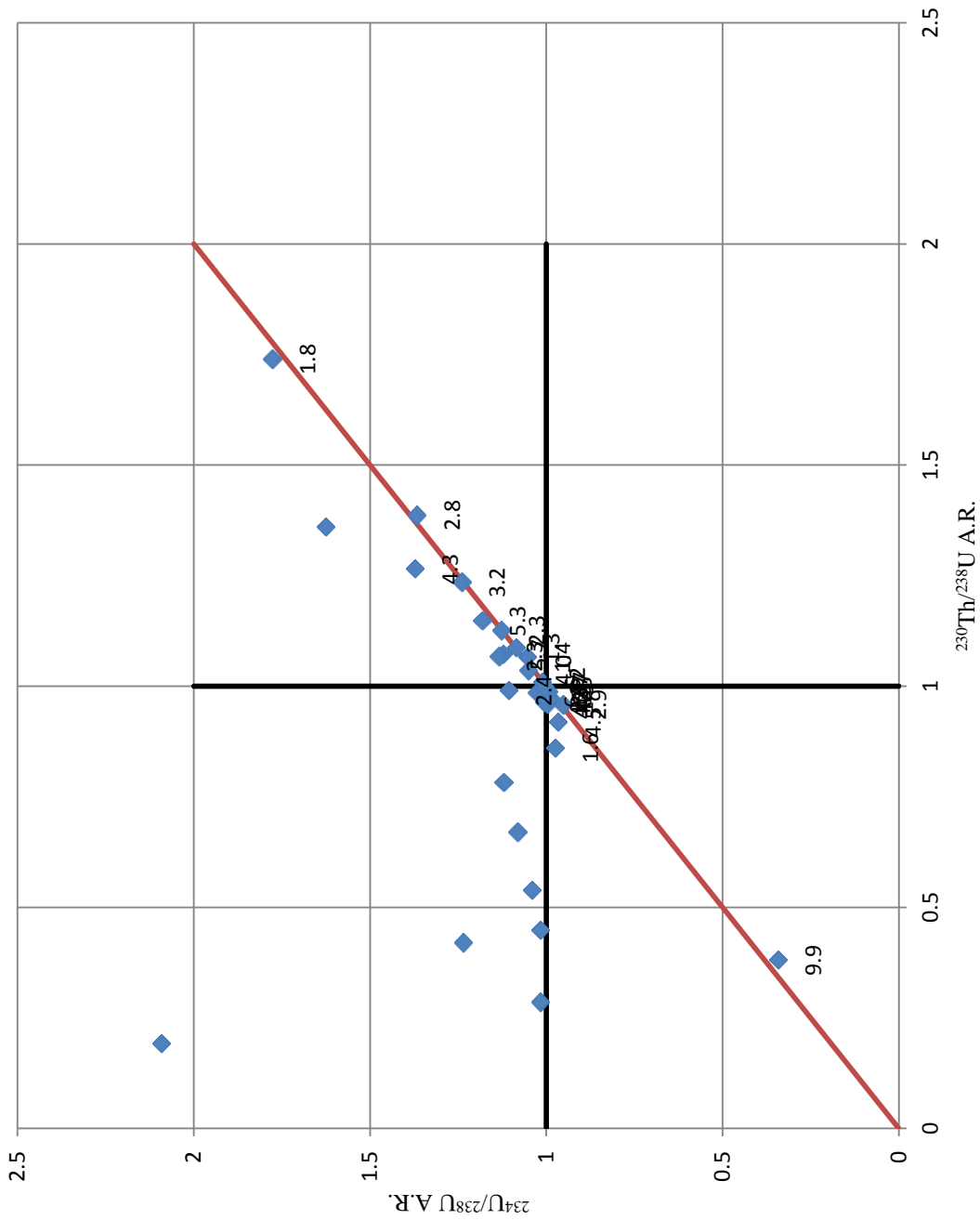
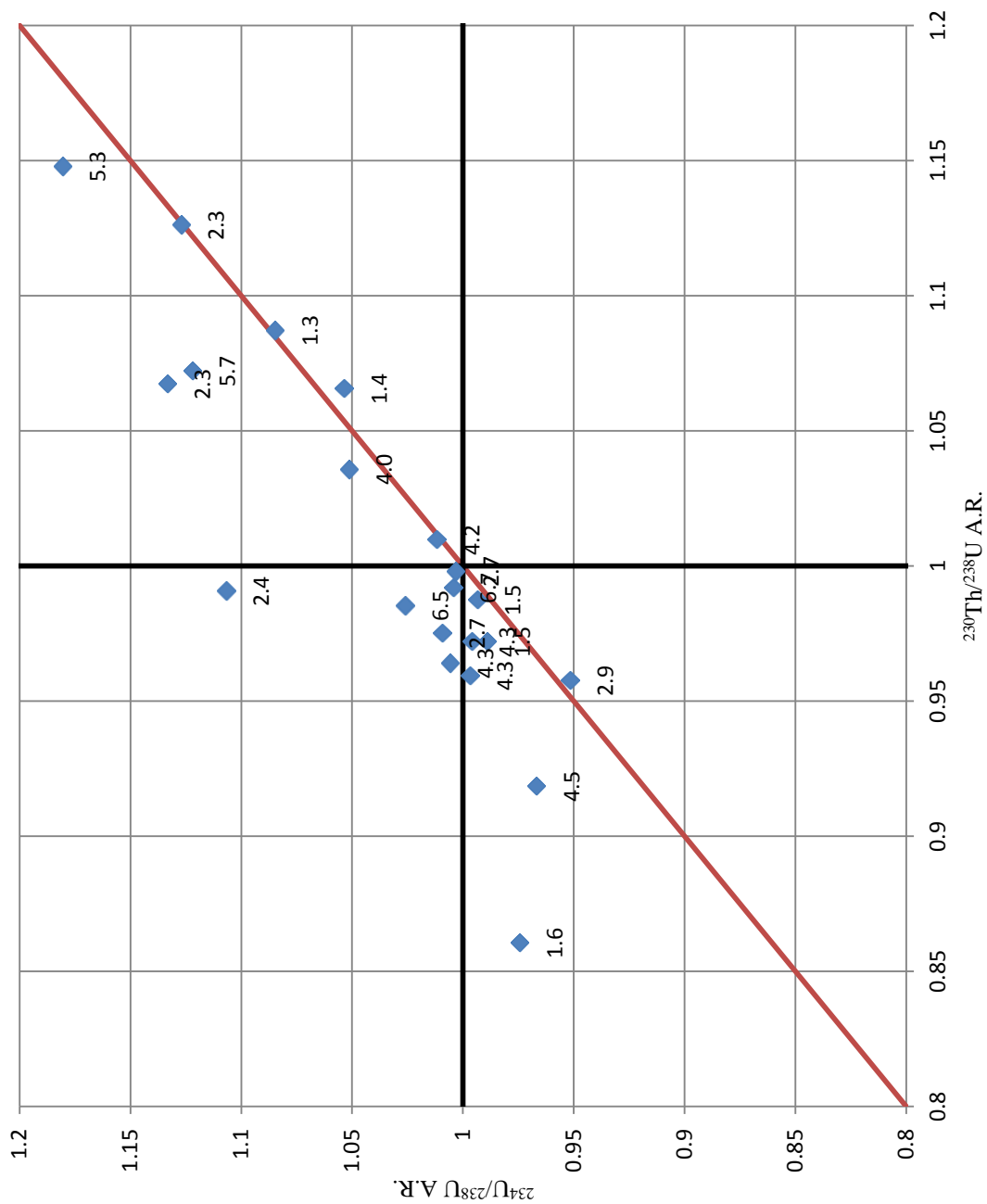**Figure 6-1.** a_{234}/a_{238} ratios for samples with $^{234}U/^{230}Th$ A.R. values between 0.85 and 1.15

Figure 6-2. a_{234}/a_{238} ratios for samples with $^{234}U/^{230}Th$ A.R. values between 0.85 and 1.15 zoomed to secular equilibrium A.R.s

Due to the inability to clearly see a trend in a-ratios in Figures 6-1 and 6-2, a theoretical balance between F-ratios and a-ratios that allow a sample to plot along the equiline was explored. That is, there is a steady state balance between the input of ^{234}U, ^{238}U, and the loss of ^{234}U and ^{238}U that allows for ^{230}Th $/^{238}U$ A.R. to be equal to ^{234}U $/^{238}U$ A.R. Assuming that input ^{234}U $/^{238}U$ A.R. can vary from 1.5 to 7.0 (range of values measured for groundwater in the Pahute Mesa vicinity; Paces et al., 2002; J.B. Paces,USGS, 2012, unpublished data), the following plots were developed for various theoretical points on the equiline.
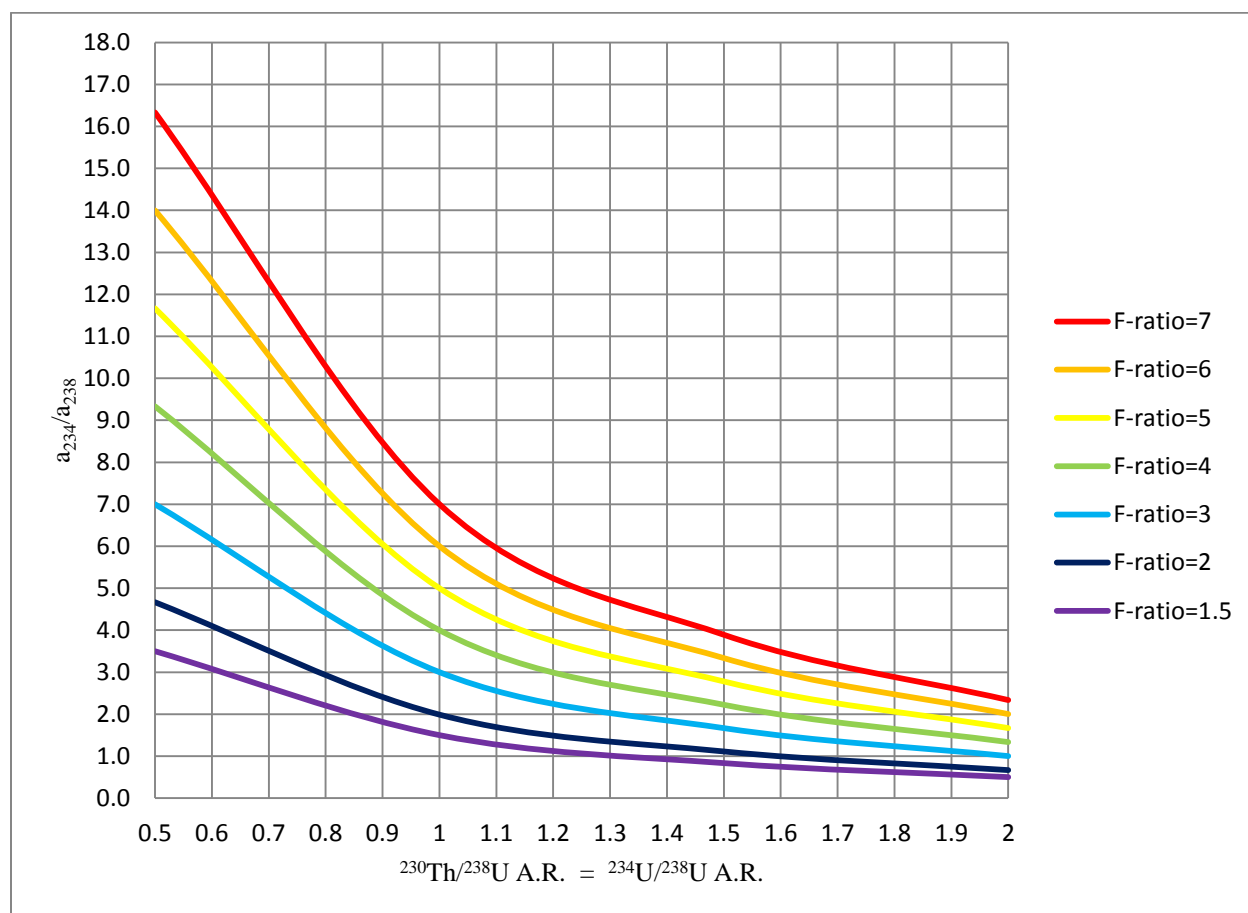
Figure 6-3. Relationship between F-ratios and a-ratios for given points on the equiline
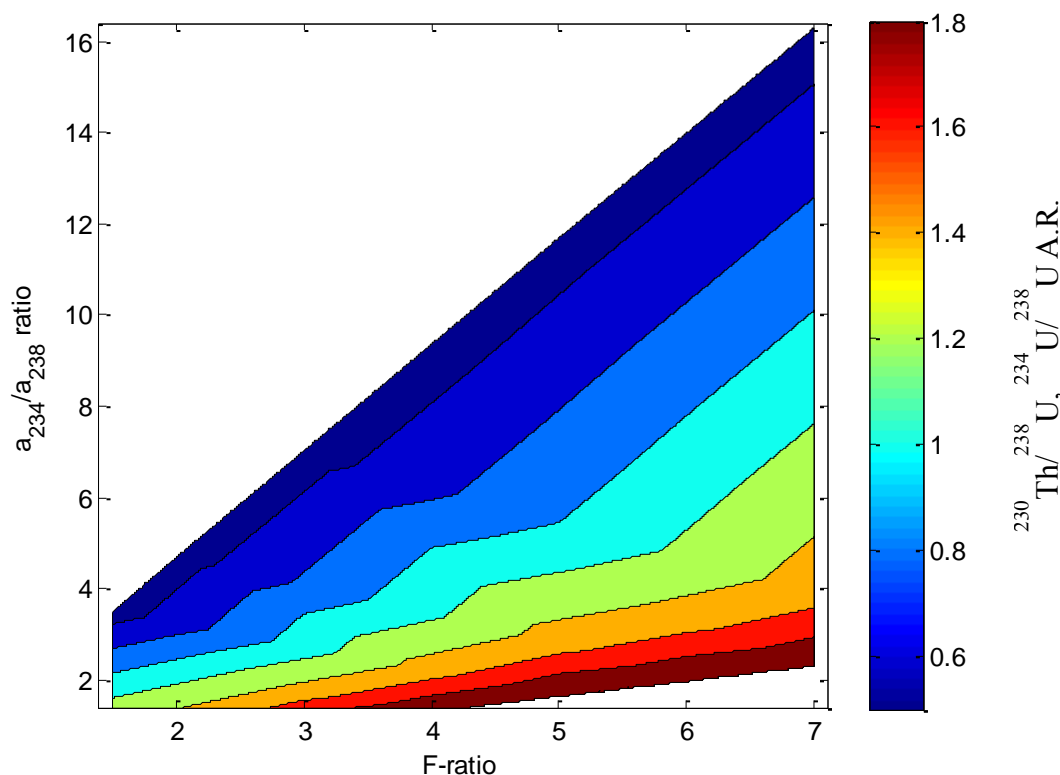
Figure 6-4. Relationship between F-ratios and a-ratios for given points on the equiline, where contours represent a sample's $^{234}U/^{238}U$ A.R.=$^{230}Th/^{238}U$ A.R.

Figures 6-3 and 6-4 show that for any given location on the equiline, a higher F-ratio corresponds to a higher a-ratio. That is, in order to maintain a position on the equiline, an increase in the input of ^{234}U to ^{238}U to the rock from the surrounding groundwater must be balanced by an increase in the loss rate of ^{234}U to ^{238}U from the rock to the groundwater. This non-linear relationship is highlighted in Figure 6-3. Moreover, in order to track movement on the equiline, if a given F-ratio remains constant, increasing the $^{234}U/^{238}U$ A.R. = $^{230}Th/^{238}U$ A.R. will require a lower a_{234}/a_{238} ratio. This shows that maintaining a greater $^{230}Th/^{238}U$ and $^{234}U/^{238}U$ A.R. requires a relatively small value of the a_{234} loss constant when compared to the a_{238} loss constant. One caveat of this analysis is that it suggests that there can exist a steady state balance of ^{234}U and ^{238}U inputs and outputs based on water-rock interaction that can result in

secular equilibrium. The model suggests that samples with U-series isotopes in secular equilibrium could theoretically indicate the presence of groundwater flow. However, this condition would require a balance between the F-ratios and a-ratios, and furthermore that this balance is maintained over about 500,000 years. Given the two possible means for obtaining the same outcome, the simpler condition (that is, the absence of groundwater flow and lack of water-rock interaction) is considered more likely. As noted earlier in this document, previous studies (Deschamps et al., 2004; Gascoyne and Miller, 2000; and Neymark et. al, 2006) interpreted rocks with U-series isotopic compositions in secular equilibrium as indicative of an absence of recent matrix water-rock interaction.

Modeling Samples' locations relative to the Equiline: Transient Conditions

While steady state conditions can be used to explain U-series isotopic compositions that plot along the equiline, a number of discrete fracture samples have $^{234}U/^{238}U$ A.R. and $^{230}Th/^{238}U$ A.R. values that plot off the equiline with $^{234}U/^{230}Th$ values greater than 1.0 (to the left of the equiline). As demonstrated by Thiel et al. (1983), points that do not fall on the equiline represent transient conditions where the system has not evolved to a steady state balance between nuclide decay, sources, and sinks. Although previous studies note that there are many possible qualitative explanations for points plotting away from the equiline with $^{234}U/^{230}Th$ A.R. values both greater and lower than 1.0 (Dequincey et al., 2002; Latham and Schwarcz, 1987; Thiel et al., 1983), most samples in this study have higher $^{234}U/^{238}U$ A.R.s relative to a given $^{230}Th/^{238}U$ A.R. In order to explain the distribution of these samples in U-series isotope space, transient solutions to

nuclide equations were developed. These numerical models closely followed formulations

developed by Dequincey et al. (2002) to simulate compositions for rocks rather than waters.

In order to get a better grasp on the physical properties that constrain the radionuclides'

concentration evolution through time, F values correspond to nuclide concentration inputs per

year. The F values represent nuclide concentration flux rates of ^{238}U and ^{234}U. Moreover, due to

the complex nature of the solutions to the ^{230}Th $/^{238}$U and ^{234}U $/^{238}$U A.R.s, it was not possible to

isolate the influence of an F-ratio as in the development of the steady state A.R. solutions. Thus

nuclide source terms are defined as a concentration per unit time [(g/g)/yr]. Through the

development of transient ^{238}U, ^{234}U and ^{230}Th concentration equations, it was assumed that input

rates of ^{234}U, ^{238}U and loss rate constants of ^{234}U and ^{238}U remained constant through time.

Variables in the transient analysis are defined in Table 6-2.

Table 6-2: Defined variables used in the development of transient U-series nuclide equations

Variable	Definition	Units
t	Time	yr
x	^{238}U concentration	(g ^{238}U/g rock)
x_0	Initial ^{238}U concentration	(g ^{238}U/g rock)
F_x	^{238}U input rate	(g ^{238}U/g water)/yr
λ_x	^{238}U decay constant	yr^{-1}
a_x	^{238}U rate loss constant	yr^{-1}
b_x	$a_x + \lambda_x$	yr^{-1}
y	^{234}U concentration	(g ^{234}U/g rock)
y_0	Initial ^{234}U concentration	(g ^{234}U/g rock)
F_y	^{234}U input rate	(g ^{234}U/g water)/yr
λ_y	^{234}U decay constant	yr^{-1}
a_y	^{234}U rate loss constant	yr^{-1}
b_y	$a_y + \lambda_y$	yr^{-1}
z	^{230}Th concentration	(g ^{230}Th/g Rock)

z_0	Initial ^{230}Th concentration	(g ^{230}Th/g Rock)
λ_z	^{230}Th decay constant	yr^{-1}

Using the above definitions given in Table 6-2, the following governing equations were derived:

$$\frac{dx}{dt} = F_x - xb_x \tag{8}$$

$$\frac{dy}{dt} = F_y + x\lambda_x - yb_y \tag{9}$$

$$\frac{dz}{dt} = y\lambda_y - z\lambda_z \tag{10}$$

The solutions to these transient equations are as shown below:

$$x(t) = x_0 e^{-b_x t} + F_x \frac{1 - e^{-b_x t}}{b_x} \tag{11}$$

$$y(t) = y_0 e^{-b_y t} + \left(F_y + \frac{F_x \lambda_x}{b_x}\right) \frac{1 - e^{-b_y t}}{b_y} + \lambda_x\left(x_0 - \frac{F_x}{b_x}\right) \frac{e^{-b_x t} - e^{-b_y t}}{b_y - b_x} \tag{12}$$

$$z(t) = z_0 e^{-\lambda_z t} + \lambda_y y_0 \frac{e^{-b_y t} - e^{-\lambda_z t}}{\lambda_z - b_y} + \left(F_y + \frac{F_x \lambda_x}{b_x}\right) \frac{\lambda_y}{b_y} \left\{\frac{1 - e^{-\lambda_z t}}{\lambda_z} - \frac{e^{-b_y t} - e^{-\lambda_z t}}{\lambda_z - b_y}\right\} + \lambda_x\left(x_0 - \right.$$

$$\left. \frac{F_x}{b_x}\right)\left(\frac{\lambda_y}{b_y - b_x}\right)\left\{\frac{e^{-b_x t} - e^{-\lambda_z t}}{\lambda_z - b_x} - \frac{e^{-b_y t} - e^{\lambda_z t}}{\lambda_z - b_y}\right\} \tag{13}$$

This then results in ^{234}U/^{238}U and ^{230}Th/^{238}U A.R.s being defined as follows:

$$\frac{^{230}Th}{^{238}U} A.R.(t) = \frac{z(t)\lambda_z}{x(t)\lambda_x} \tag{14}$$

$$\frac{^{234}U}{^{238}U} A.R.(t) = \frac{y(t)\lambda_y}{x(t)\lambda_x} \tag{15}$$

Input values in the solutions to the transient equations were based on the A.R.s and U

concentrations in groundwaters (Paces et al., 2002; J.B. Paces, USGS, unpublished data).

$^{234}U/^{238}U$ A.R.s chosen for this exercise ranged from 2.0 to 6.0 while groundwater U

concentrations ranged from 0.5E-9 to 5E-9 (g/g) and remained constant in time. This allowed us

to define inputs to the system:

$$F_x = {}^{238}Uwater \tag{16}$$

$$F_y = \left({}^{234}U/{}^{238}U \, A.R. water \right)\left({}^{238}Uwater\right)\left(\frac{\lambda_x}{\lambda_y}\right) \tag{17}$$

It is acknowledged that in order for unit consistencies in equations 8 and 9, F_x and F_y are

defined in (g/g)/yr. While isotopic data for groundwaters on Pahute Mesa does not include the

element of time (data regarding U-series isotopic compositions through time is not available), it

was important to include information from groundwater compositions, as they represent the

source terms for radionuclides into the rock system. This approach, however, resulted in

assuming water U concentrations and $^{234}U/^{238}U$ A.R.s corresponded to nuclide input fluxes of

(g/g)/yr. Further simplifying the model, it was assumed that the groundwater and bulk rock U

concentration represented only the ^{238}U isotopic concentration. This assumption is consistent

with Lounsbury (1956) where ^{238}U was found to have a natural abundance in excess of 99%.

Bulk rock U concentrations were used to constrain initial concentrations of ^{238}U, ^{234}U, and ^{230}Th

in the system. Based on measured values given in Table 5-1, rock ^{238}U concentrations used in

models ranged from 2E-6 to 10E-6. These measured values of ^{238}U concentrations formed the

basis for the chosen initial condition of x_0. Values of y_0 and z_0 were based on the value of x_0 and

selected initial $^{230}Th/^{238}U$ and $^{234}U/^{238}U$ A.R.s. Values of a_{234} and a_{238} were constrained by

choosing an a-ratio within the range of the values given in Table 6-3 and then choosing an a_{234}

value similar to those fitted in Dequincey et al. (2002), which were on the order of 1E-6 and 1E-5 yr^{-1}.

As seen in Figure 6-1, data that are not clustered along the equiline fall into two regions: 1) to the left of the equiline along a trend with $^{234}U/^{238}U$ A.R. values of about 1.0–1.2 and $^{230}Th/^{238}U$ A.R. values between about 0.3 and 1.0, and 2) the data point that lies at $^{230}Th/^{238}U$ A.R. = 0.191 and $^{234}U/^{238}U$ A.R. = 2.09. These data points were modeled using two different starting conditions: (A) the fracture surface was initially in secular equilibrium and was then exposed to a constant influx of groundwater containing various U concentrations and $^{234}U/^{238}U$ A.R. values, and (B) as a very young fracture surface coating with $^{234}U/^{238}U$ A.R. inherited from the groundwater and no initial ^{230}Th. Different scenarios used to capture the data in 1) and 2) and the initial conditions of the fracture surface described in A) and B) are explored in the following tables and figures. In Figures 6-5 through 6-22 blue asterisks (*) represent isotopic compositions at a time interval of 1,000 years, green asterisks (*) represent A.R. values at 10,000 years, red asterisks (*) represent A.R. values at 100,000 years, and magenta asterisks (*) represent A.R. values close to steady state conditions. The solid black lines correspond to the equiline. For the purpose of this thesis, steady sate conditions were said to be reached at the nearest 10,000 years when there was less than a 0.1% change in successive transient $^{234}U/^{238}U$ and $^{230}Th/^{238}U$ A.R.s. In the following table and figures, input parameters where changed one by one. In the following tables, black colored inputs remained constant while blue, green, and red inputs corresponded to the same colored lines shown in the related figure. In Table 6-3, Figures 6-5 through 6-9 represent possible explanations for data plotting to the left of the equiline in a system starting in secular equilibrium, while Figures 6-10 through 6-14 represent possible explanations for the data point plotting at $^{230}Th/^{238}U$ A.R. =0.191 and $^{234}U/^{238}U$ A.R.=2.09. Figures 6-5 through 6-14

demonstrate that there is a whole host of input paramters that can be employed to explain a rock sample's relationship to the equiline. While these parameters can vary greatly, they are restricted to producing results with $^{234}U/^{230}Th$ A.R.s above the equiline and above the $^{234}U/^{238}U$ A.R. =1.0 line.

It is important to note that while many of the figures on the following pages show that steady state conditions result in secular equilibrium, this is coincidental and is a result of choosing a_{234}/a_{238} ratios that matched groundwater $^{234}U/^{238}U$ A.R.s. In reality, in this model any point along the equiline represents a rock surface that is in isotopic equilibrium with the surrounding groundwater.

Table 6-3. Input parameters to equations 11, 12, and 13 resulting in differing U-series transient behavior for initial condition of $^{230}\text{Th}/^{238}\text{U}$ A.R. = 1.0

| Figure #	Water $^{234}\text{U}/^{238}\text{U}$ A.R.	U Conc. water (ppb)	U Conc. rock (ppm)	a_{234}/a_{238}	a_{234} ($10^{-4}\,\text{yr}^{-1}$)	Time to steady state ($10^5\,\text{yr}$)	Explanation
6-5	2 4 6	2	3	2	1	5.0 5.0 5.0	Increase in the $^{234}\text{U}/^{238}\text{U}$ A.R. of the water results in higher $^{234}\text{U}/^{238}\text{U}$ A.R. values and higher $^{230}\text{Th}/^{238}\text{U}$ A.R. values at steady state.
6-6	2	0.5 2 5	3	2	1	4.7 5.0 5.0	Increase in the ^{238}U concentration of the water causes sample A.R.s to move further away from secular equilibrium toward the A.R in the water.
6-7	2	2	2 5 10	2	1	5.0 4.9 4.7	Increase in the ^{238}U concentration in the rock results in sample A.R.s that are less impacted by nuclide inputs from the water.
6-8	2	2	3	1.5 2 3	1	5.0 5.0 5.0	Increase in the a_{234}/a_{238} ratio, which gives higher preferential leaching of ^{234}U, results in lower steady state values of $^{234}\text{U}/^{238}\text{U}$ and $^{230}\text{Th}/^{238}\text{U}$ A.R. values.
6-9	2	2	3	2	5 0.5 0.05	4.8 5.1 12.2	Increase in the absolute value of a_{234} results in lower $^{234}\text{U}/^{238}\text{U}$ A.R.s throughout the sample's transition to steady state.
6-10	2 4 6	2.5	2	4	5	5.0 5.0 5.0	Increase in the $^{234}\text{U}/^{238}\text{U}$ A.R. of the water results in higher $^{234}\text{U}/^{238}\text{U}$ A.R. values and higher $^{230}\text{Th}/^{238}\text{U}$ A.R. values at steady state.
6-11	4	1 5 10	2	4	5	4.7 4.9 4.9	Increase in the ^{238}U concentration of the water causes sample A.R.s to move further away from secular equilibrium toward the A.R in the water
6-12	4	2.5	2 5 10	4	5	4.9 4.7 4.2	Increase in the ^{238}U concentration of the rock results in sample A.R.'s that are less impacted by nuclide inputs from the water.
6-13	4	2.5	2.5	2.5 4 6	5	4.8 4.8 4.8	Increase in the a_{234}/a_{238} ratio, which gives higher preferential leaching of ^{234}U, results in lower steady state values of $^{234}\text{U}/^{238}\text{U}$ and $^{230}\text{Th}/^{238}\text{U}$ A.R. values.
6-14	4	2.5	2.5	4	1 5 9	5.0 4.8 4.7	Increase in the absolute value of a_{234} results in lower $^{234}\text{U}/^{238}\text{U}$ A.R.s through the transition to steady state but gives similar values for $^{230}\text{Th}/^{238}\text{U}$ A.R.s.
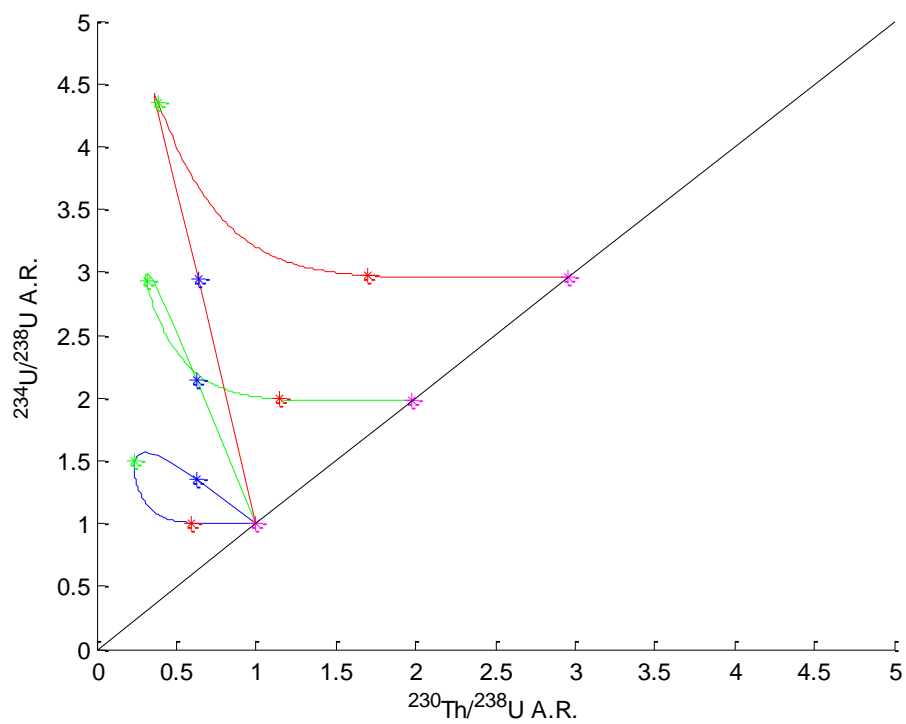
Figure 6-5. Illustration of impact of changing water ^{234}U/^{238}U A.R for case 1A
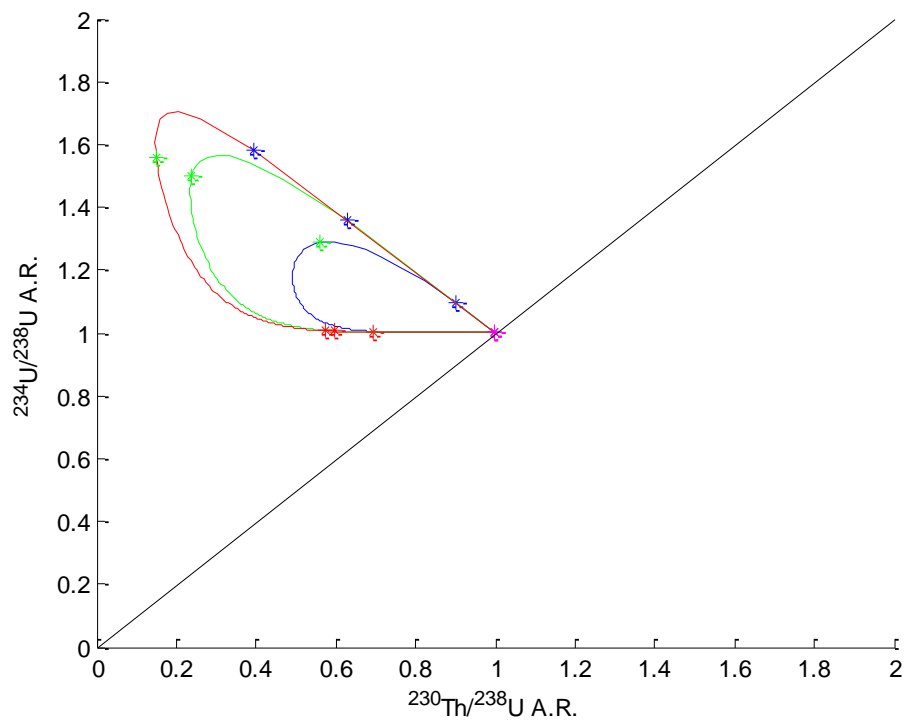

Figure 6-6. Illustration of the impact of changing ^{238}U water concentrations for case 1A
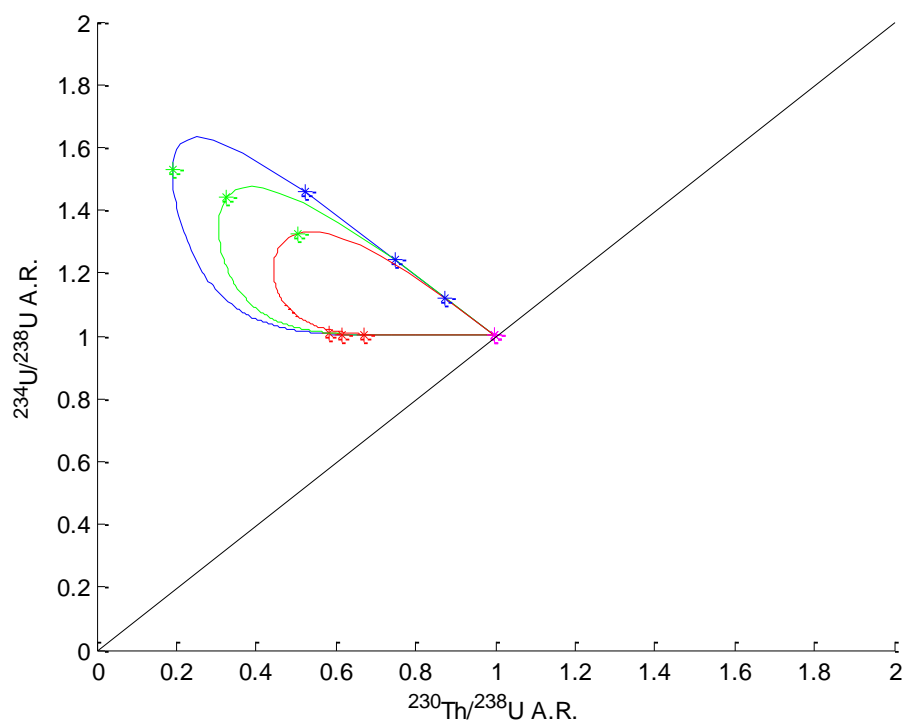
Figure 6-7. Illustration of the impact of changing ^{238}U rock concentrations for case 1A
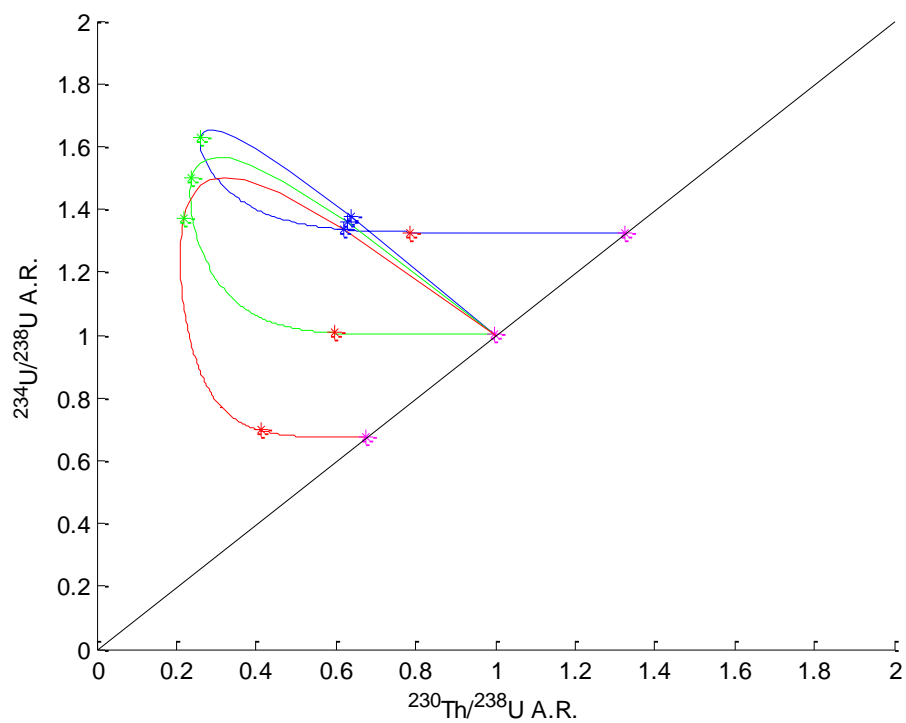

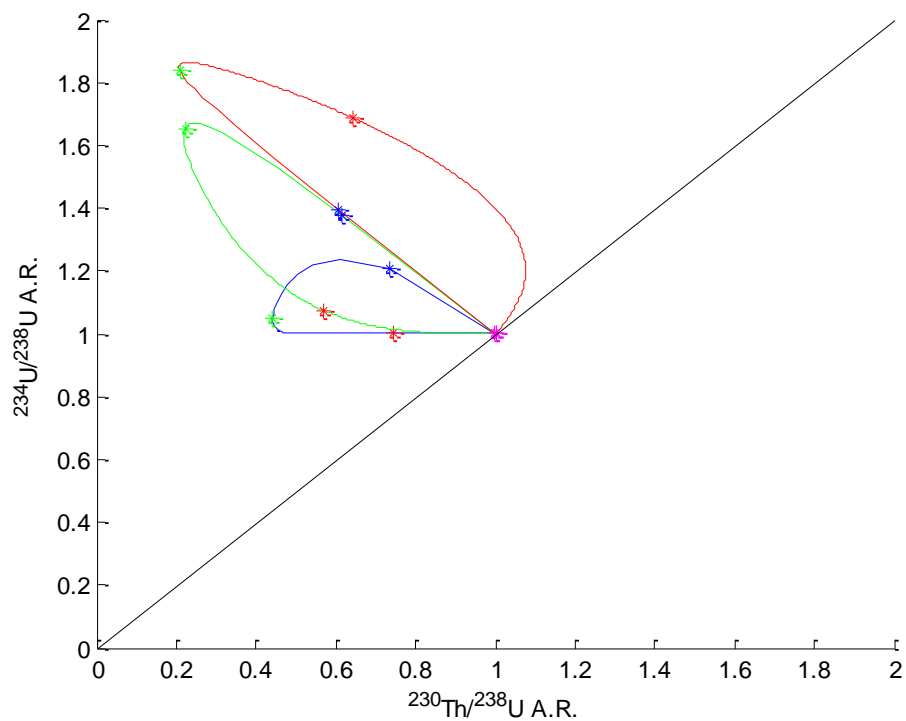**Figure 6-8. Illustration of the impact of changing the a_{234}/a_{238} ratio for case 1A**

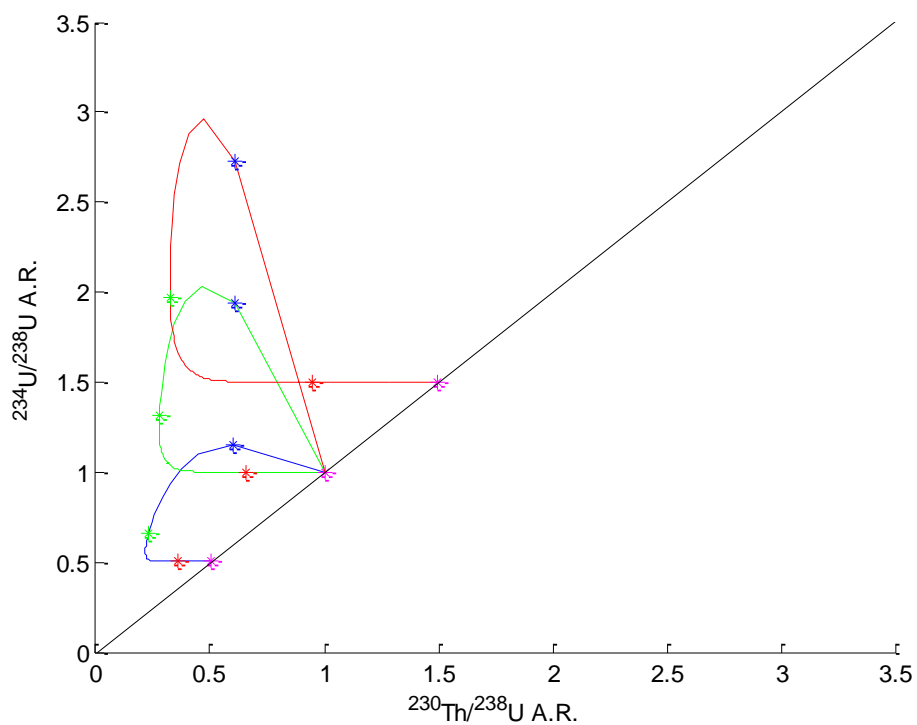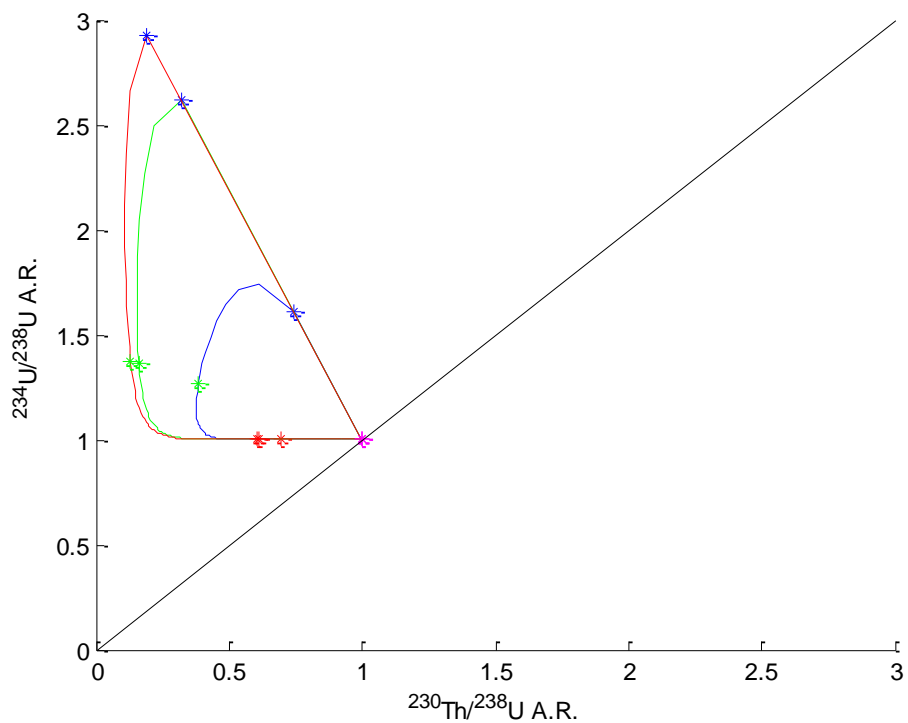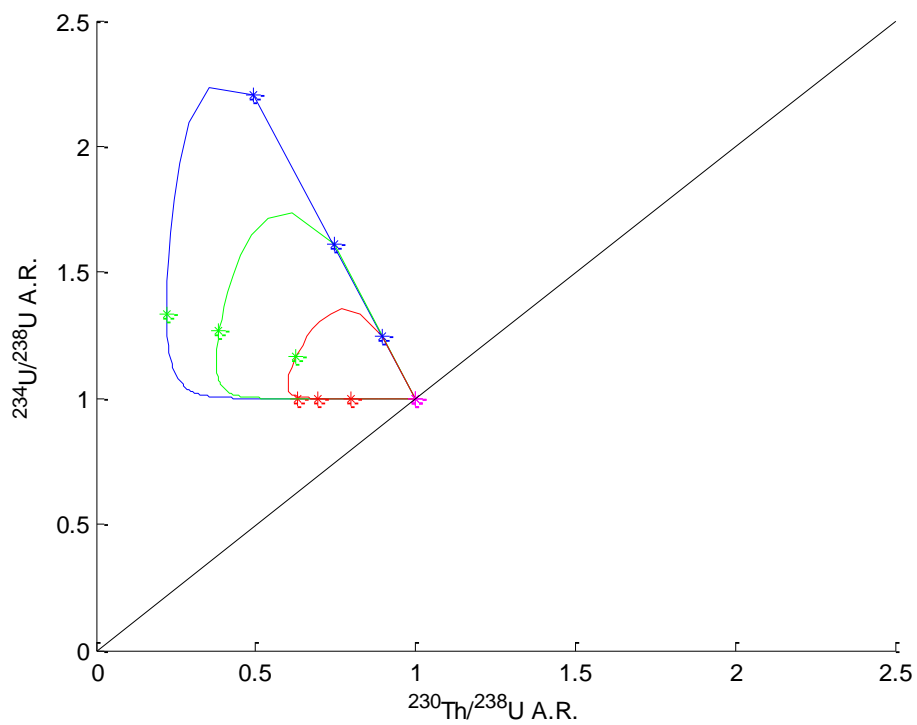**Figure 6-9. Illustration of the impact of changing the absolute value of a$_{234}$ for case 1A**

Figure 6-10. Illustration of impact of changing water ^{234}U/^{238}U A.R. for case 2A

Figure 6-11. Illustration of the impact of changing ^{238}U water concentrations for case 2A

Figure 6-12. Illustration of the impact of changing ^{238}U rock concentrations for case 2A
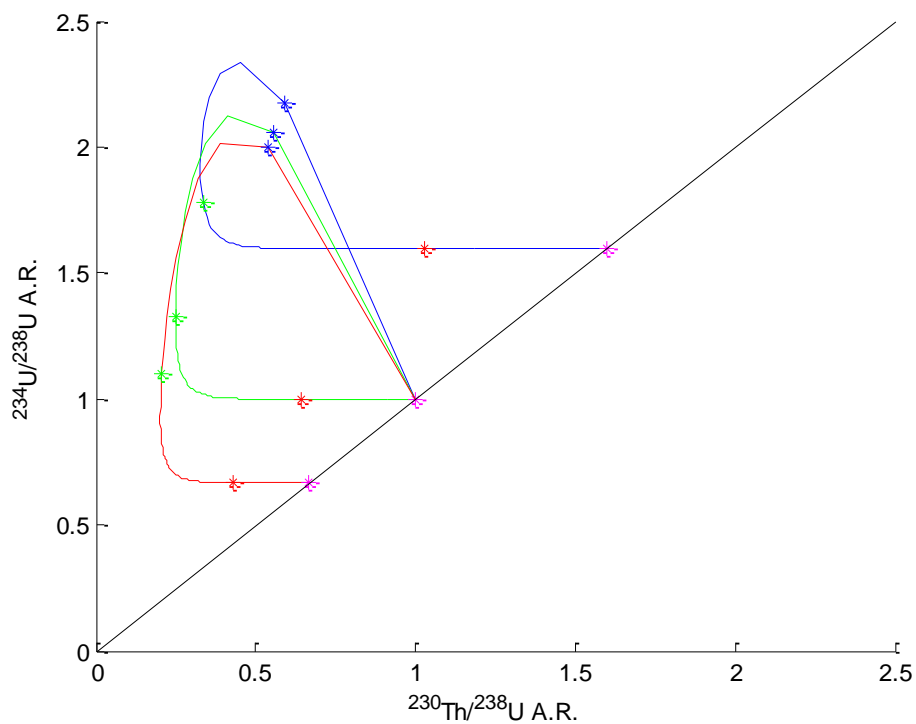
Figure 6-13. Illustration of the impact of changing the a_{234}/a_{238} ratio for case 2A
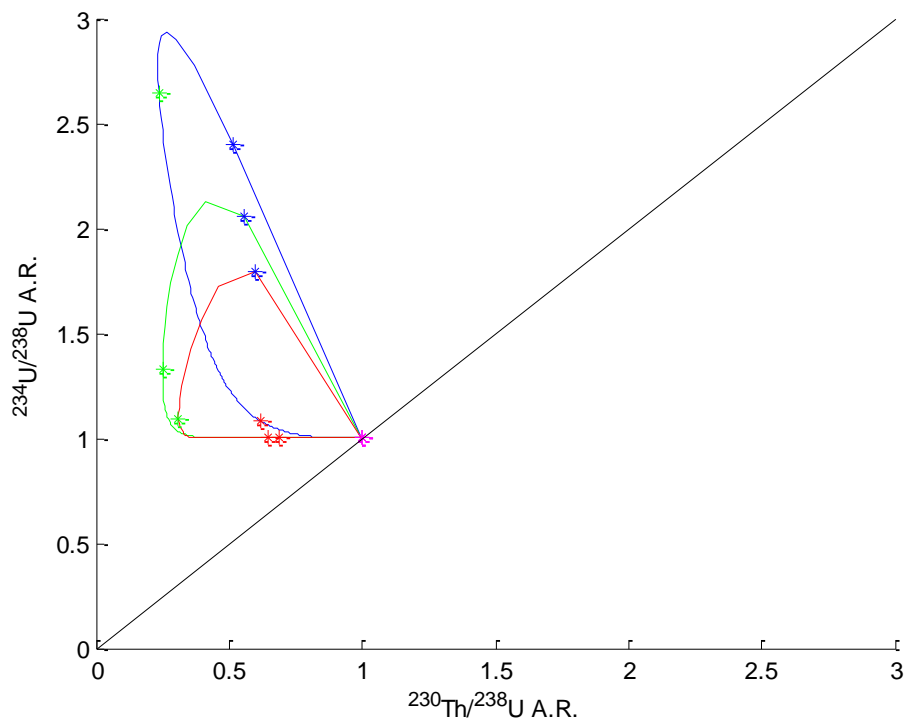

Figure 6-14. Illustration of the impact of changing the absolute value of a_{234} for case 2A

Table 6-4 and the following 8 figures give possible scenarios for transient solutions to the $^{230}\text{Th}/^{238}\text{U}$ and $^{234}\text{U}/^{238}\text{U}$ A.R.s starting with an initial condition of the discrete fracture surface representing a newly deposited mineral coating where ^{234}U has not had sufficient time to decay and the starting $^{230}\text{Th}/^{238}\text{U}$ A.R. for the rock, in this case, the newly formed fracture mineral, is equal to 0. In order for this to be a reasonable assumption, the initial $^{234}\text{U}/^{238}\text{U}$ A.R. in the rock should be equivalent to the $^{234}\text{U}/^{238}\text{U}$ A.R. in the water. In order to generate scenarios to match the data described in in 1B and 2B, a value of $^{234}\text{U}/^{238}\text{U}$ A.R.=2.2 was chosen. In Table 6-4, Figures 6-15 through 6-18 represent solutions corresponding to 1B and Figures 6-19 through 6-22 represent the solutions corresponding to 2B.

Table 6-4. Input parameters to equations 11, 12, and 13 resulting in differing U-series transient behavior for initial condition of ^{230}Th/^{238}U A.R. = 0

| Figure #	Water ^{234}U/^{238}U A.R.	U Conc. water (ppb)	U Conc rock (ppm)	a_{234}/a_{238}	a_{234} (10^{-4} yr^{-1})	Time to steady state (10^5 yr)	Explanation
6-15	2.2	1 2 5	3	2	0.9	5.0 5.1 5.1	Increasing the ^{238}U concentration in the water has a negligible impact on the behavior of the ^{230}Th/^{238}U and ^{234}U/^{238}U A.R. solutions.
6-16	2.2	2	2 5 10	2	0.9	5.1 5.0 4.9	Increasing the ^{238}U concentration in the water has a negligible impact on the behavior of the ^{230}Th/^{238}U and ^{234}U/^{238}U A.R. solutions. It reduces the time to steady state, however.
6-17	2.2	2	3	1.9 2.3 2.7	0.9	5.0 5.1 5.1	Increasing the a_{234}/a_{238} ratio results in lower values of ^{230}Th/^{238}U and ^{234}U/^{238}U A.R. through time and at steady state.
6-18	2.2	2	3	2	1 0.5 0.1	5.0 5.2 7.2	The absolute value of a_{234} greatly impacts the solution. Lower values of a_{234} correspond to higher ^{234}U/^{238}U A.R.s.
6-19	2.2	1 2 5	3	3	0.1	9.5 9.5 9.5	Increasing the ^{238}U concentration in the water has a negligible impact on the behavior of the ^{230}Th/^{238}U and ^{234}U/^{238}U A.R. solutions.
6-20	2.2	2	2 5 10	3	0.1	9.5 9.5 9.5	Increasing the ^{238}U concentration in the rock has a negligible impact on the behavior of the ^{230}Th/^{238}U and ^{234}U/^{238}U A.R. solutions
6-21	2.2	2	3	1.5 3.0 4.5	0.1	5.7 9.4 12.2	Increasing the a_{234}/a_{238} ratio results in lower values of ^{230}Th/^{238}U and ^{234}U/^{238}U A.R. through time and at steady state .
6-22	2.2	2	3	3	1 0.1 0.01	5.0 9.5 18.8	Decreasing the absolute value of a_{234} greatly impacts the evolution of ^{230}Th/^{238}U and ^{234}U/^{238}U A.R.s and results in higher values of ^{234}U/^{238}U A.R.
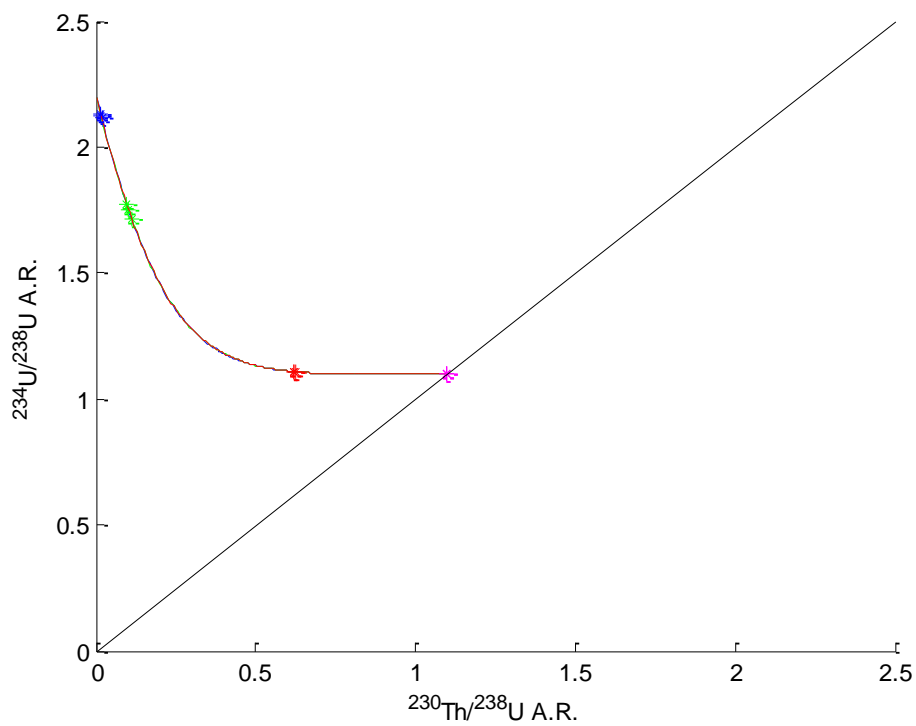
Figure 6-15. Illustration of the impact of changing ²³⁸U water concentrations for case 1B
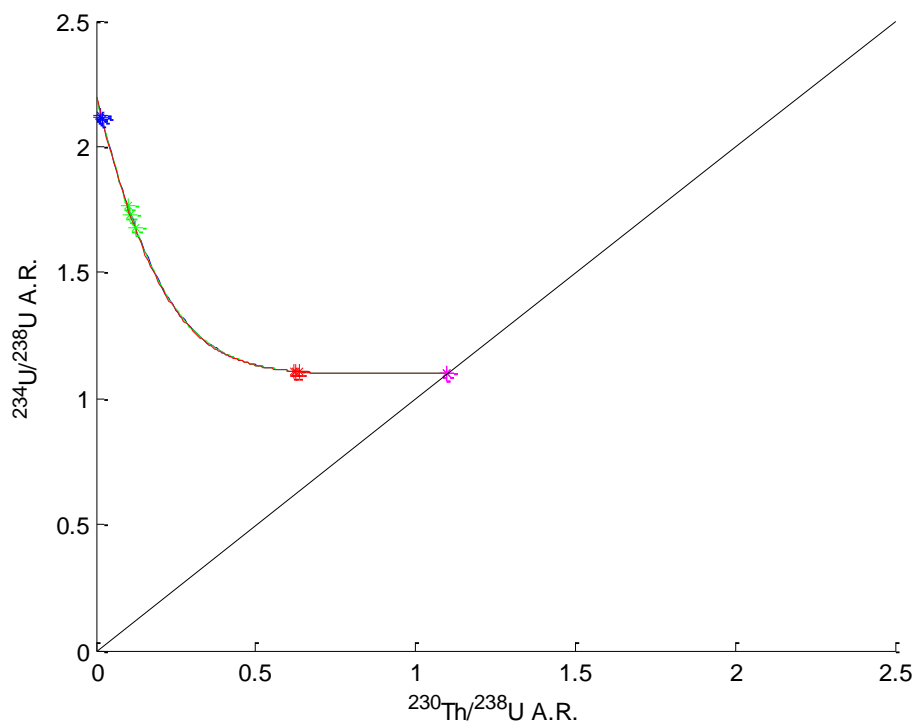

Figure 6-16. Illustration of the impact of changing ²³⁸U rock concentrations for case 1B
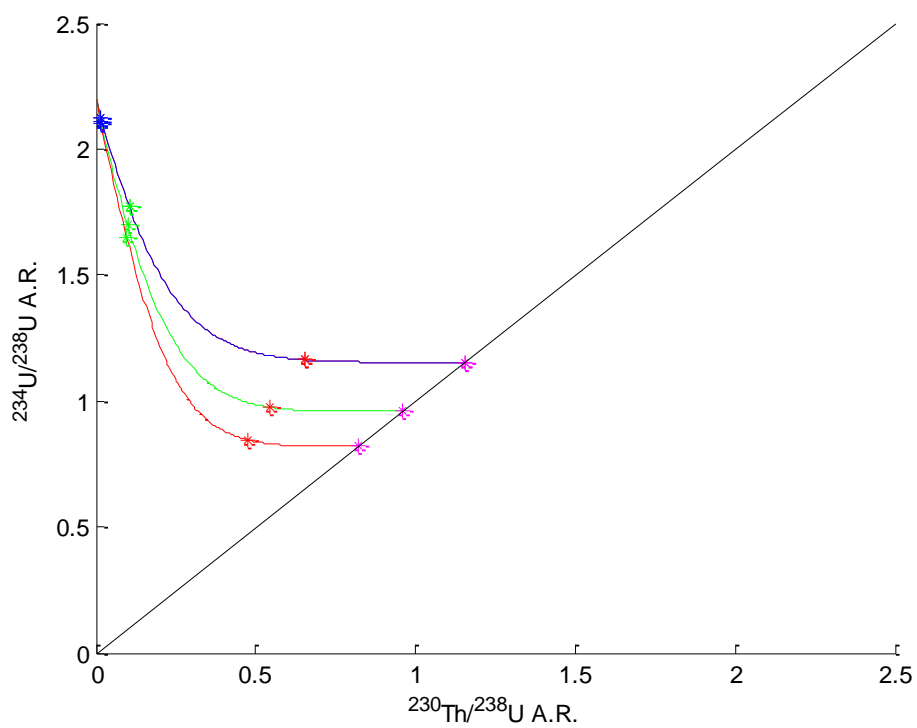
Figure 6-17. Illustration of the impact of changing the a$_{234}$/a$_{238}$ ratio for case 1B
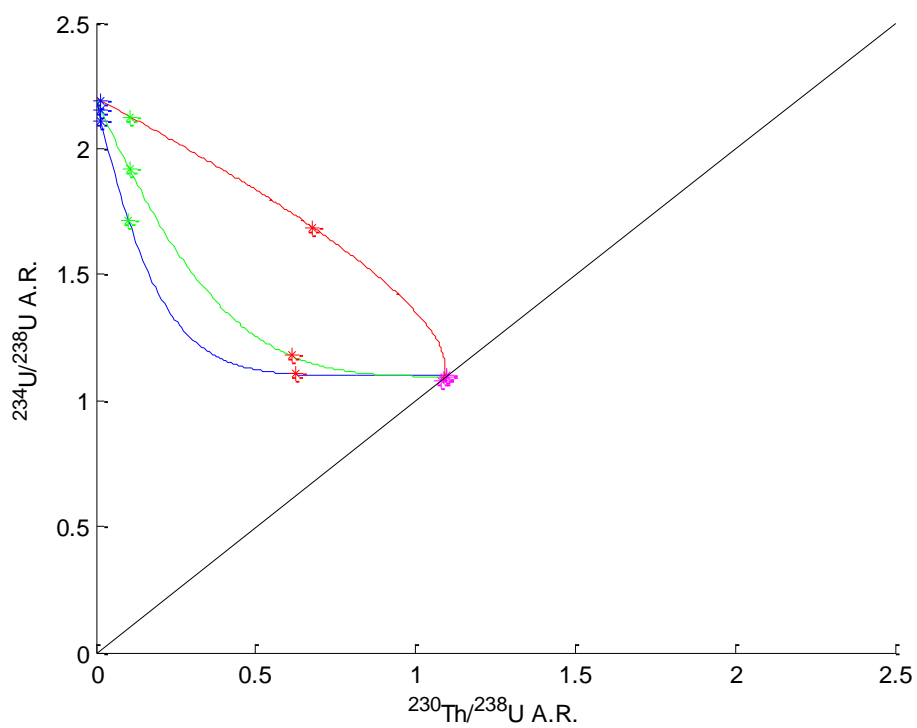

Figure 6-18. Illustration of the impact of changing the absolute value of a$_{234}$ for case 1B
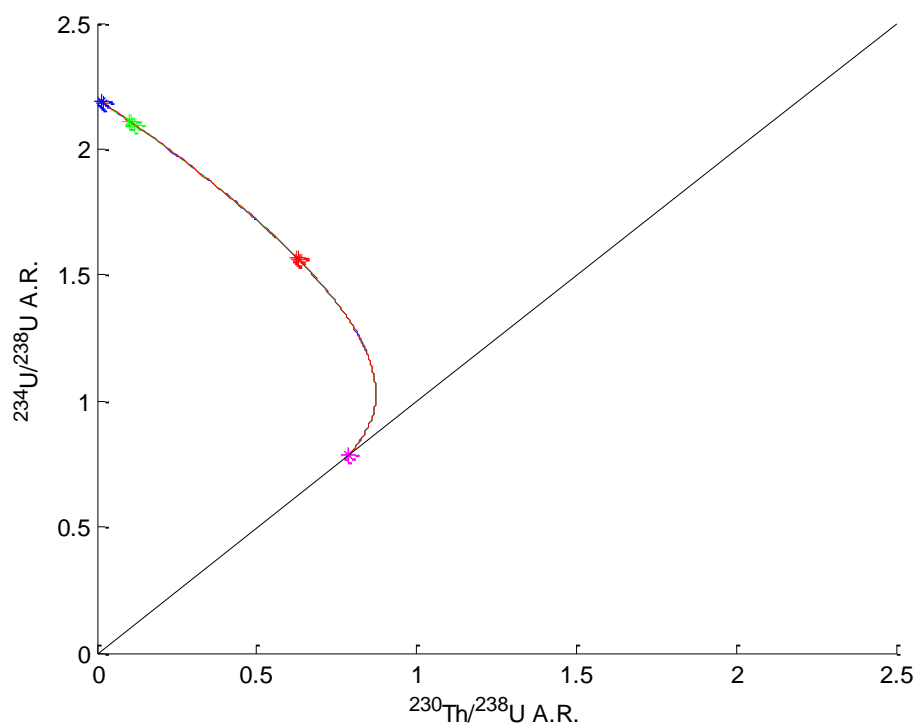
Figure 6-19. Illustration of the impact of changing ²³⁸U water concentrations for case 2B
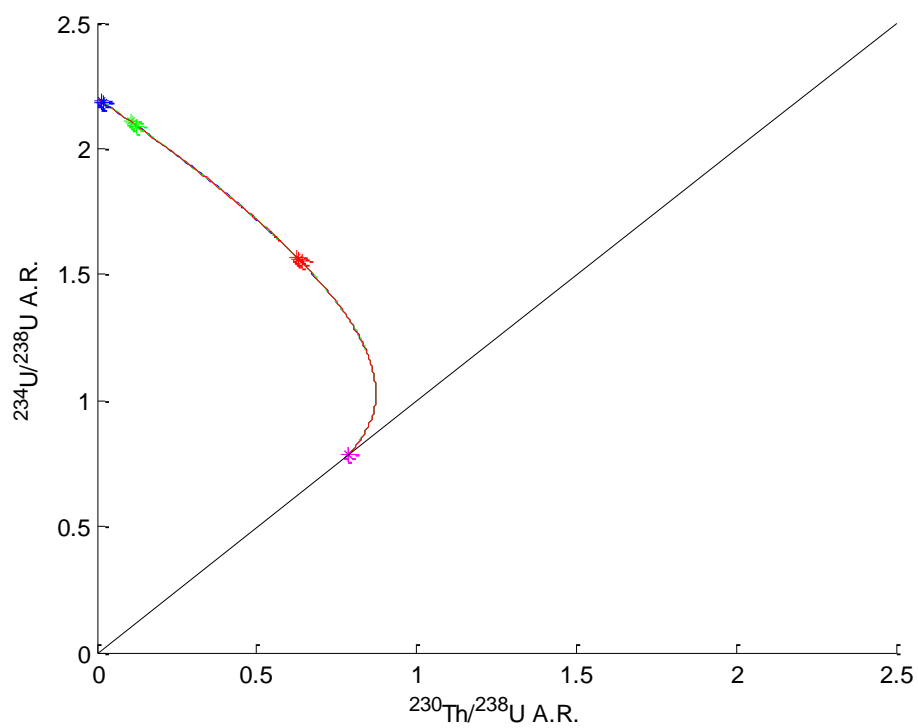

Figure 6-20. Illustration of the impact of changing ²³⁸U rock concentrations for case 2B
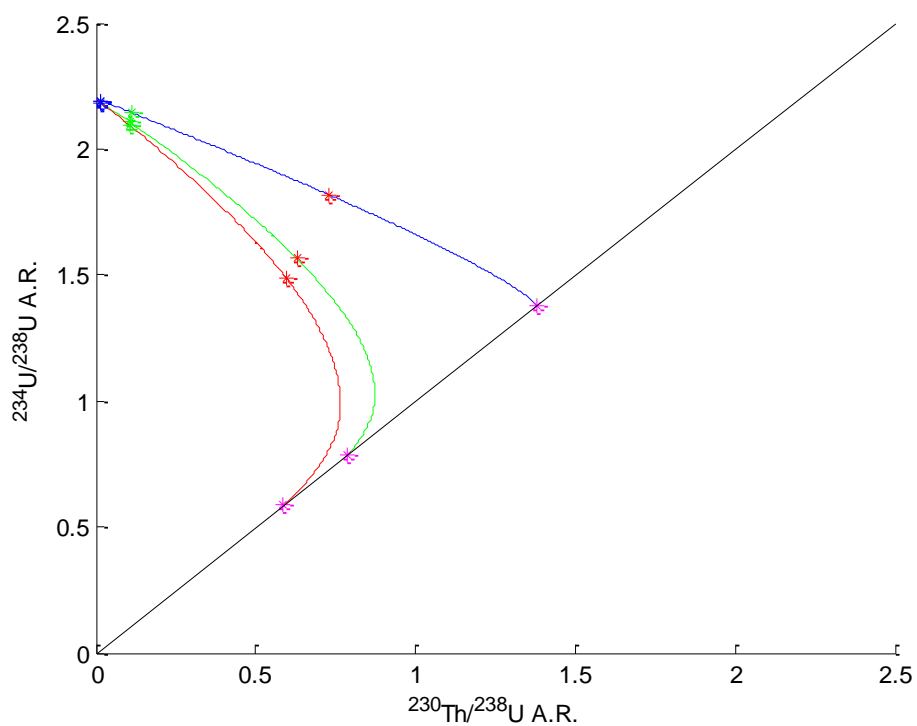
Figure 6-21. Illustration of the impact of changing the a_{234}/a_{238} ratio for case 2B
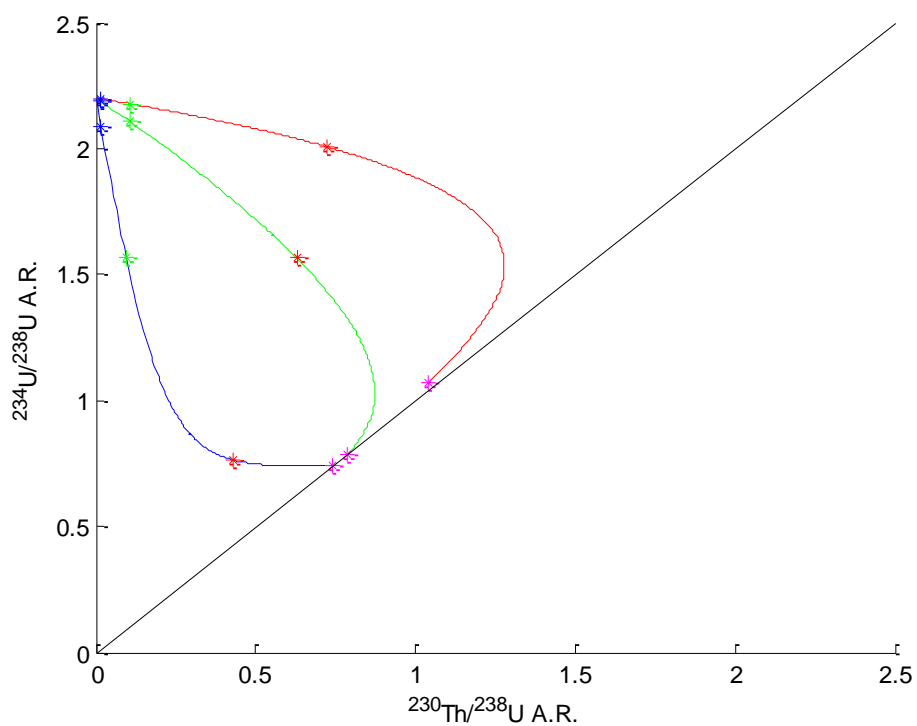

Figure 6-22. Illustration of the impact of changing the absolute value of a_{234} for case 2B

Equiline Modeling Considerations for Wafer Profiles

As previously explored, modeling about the equiline can be used to gain insight into whether rock samples' A.R.s can be considered to be at a steady state or if they need to be modeled as changing in time. This modeling approach can be applied data from wafer profiles presented in Chapter 5. Figure 6-23 suggests that interior samples at UE-19fs: 5211' can be modeled as being in steady state while the fracture surface clearly bears the signature of a relatively recent water-rock interaction. A similar analysis applies for wafers from UE-19gs: 4658', except that the first wafer, in addition to the fracture surface, needs to be modeled as being in a transient state. In sharp contrast, the fracture surface and the first wafer from UE-20f: 2849' suggest a steady state balance of ^{234}U and ^{238}U sources and sinks while interior wafers suggest the presence of a U-depleted system. In addition to all wafer samples, the fracture surface at PM-1: 6084' can be modeled as being in steady state since it too lies on the equiline. Wafer samples plotting on the equiline suggest that a steady state diffusive model would be appropriate to explain ^{230}Th/^{238}U and ^{234}U/^{238}U A.R.s.
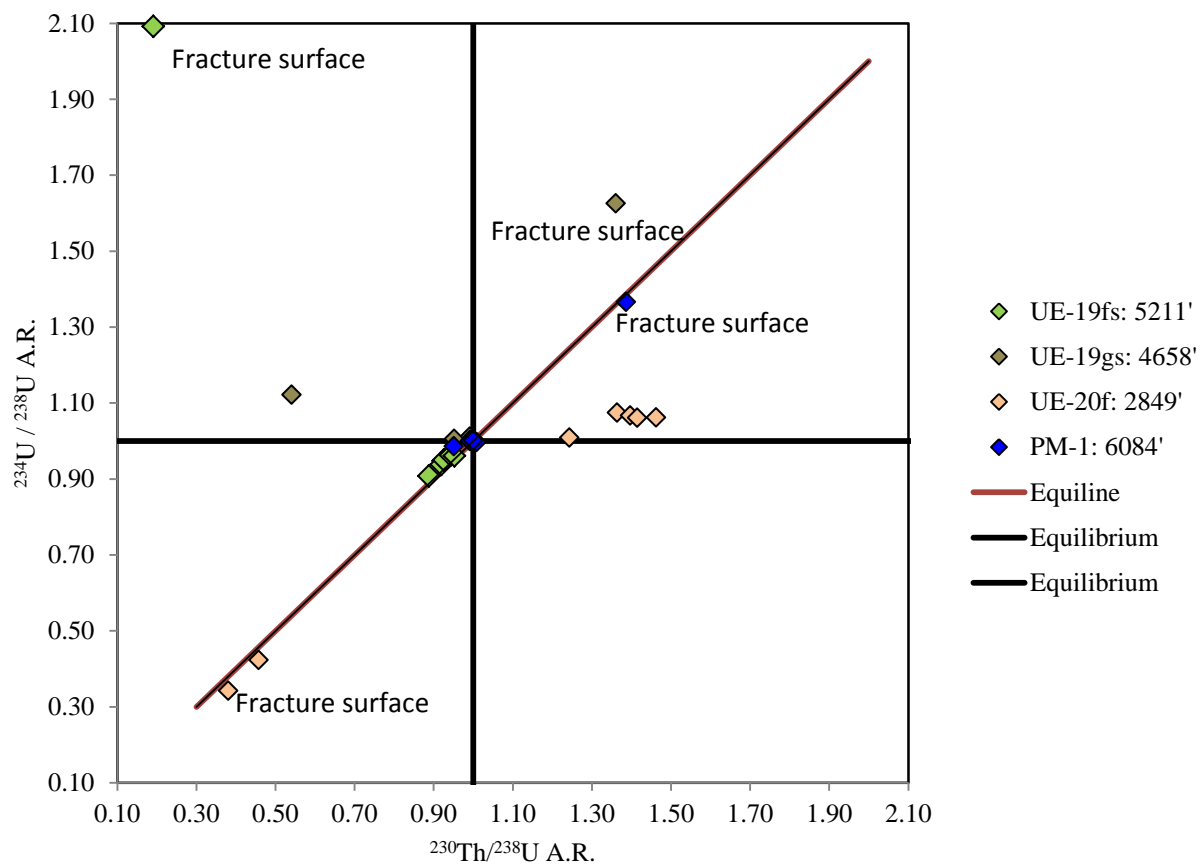
Figure 6-23. U-series isotopic compositions of wafer samples and their relation to the equiline

CHAPTER 7

CONCLUSION AND SUGGESTION FOR FUTURE WORK

This thesis investigates the use of isotopes in the U-series decay chain to provide insight into the hydrogeological history of the NNSS. Specifically, data obtained in this project show that the majority of discrete fracture surfaces sampled show radioactive disequilibrium for ^{230}Th/^{238}U and ^{234}U/^{238}U A.R.s, which is interpreted as evidence of water-rock interaction in the last 500,000 years. While this thesis did not model discrete fracture distribution in aquifer units at Pahute Mesa, it showed that 24 out of 33 discrete fractures analyzed had isotopic ratios that deviated more than 2% from secular equilibrium. This suggests that ~73% of the discrete fracture surfaces analyzed are exposed to recent groundwater flow. This could provide a means for better characterizing the percentage of fractures in flow models that are significant. That is, we have shown that ~73% of the discrete fracture surfaces contribute to the concept of secondary permeability. In contrast, most samples of interior intact core and brecciated/rubblized core tend to cluster around values of radioactive secular equilibrium. These observations are consistent with the well-established concept that groundwater flow at Pahute Mesa is dominated by secondary permeability in the form of a network of discrete fractures.

As seen in Chapter 6 of this thesis, samples that have equal ^{230}Th/^{238}U and ^{234}U/^{238}U A.R.s and thus lie on the equiline, are likely the result of a steady state balance between the loss and gain of ^{234}U and ^{238}U isotopes. Moreover, samples that lie on the equiline represent a balance between the ratio of ^{234}U/^{238}U inputs and outputs. This represents the majority of the samples analyzed in this study. Alternatively, a smaller number of samples plot to the left of the equiline with ^{234}U/^{230}Th A.R. > 1.0. Discrete fracture samples showing these relations are indicative of a system that is in a transient state. This suggests that there has been a change in the addition or

loss rate of ^{234}U or ^{238}U nuclides to the rock matrix in the relatively recent past (within the last 500,000 years). Therefore, samples falling on the equiline at distances more than about 2% away from secular equilibrium or that fall to the left of the equiline suggest recent water-rock interaction in an actively flowing groundwater system. The fact that nearly all rock samples have ^{234}U/^{238}U A.R. and ^{230}Th/^{238}U A.R. values greater than 1.0 is interpreted as evidence of a system where U is enriched, indicating that rocks show a net gain of U from groundwater. Models of U-series isotope evolution consider both steady state and transient conditions have been developed and are able to use observed data for various concentrations and isotope compositions in groundwater and rock matrix to explain points that fall along the equiline as well as to the left of the equiline.

Future work should focus on better mineralogical characterization of rock samples in order to better constrain parameters used in numerical models and to better understand the physical and mineralogical controls leading to radioactive disequilibrium at Pahute Mesa. Similarly, the ability to better constrain these values should lead to the successful development of a diffusion-based model to characterize ^{230}Th/^{238}U and ^{234}U/^{238}U A.R. values as a function of distance into the rock matrix from an actively flowing fracture surface. This diffusion-based model should be developed in a transient state as opposed to the steady state approach that was attempted in this thesis. A transient model is essential because rock matrix material at distances away from the fracture surface is likely still progressing to steady state A.R.s given the large time scales of diffusion in rock

REFERENCES

Blankennagel, R.K. and Weir, J.E., Jr., (1973). "Geohydrology of the Eastern Part of Pahute Mesa, Nevada Test Site, Nye County, Nevada." *United States Department of Energy Internal Report: U.S. Atomic Energy Commission, U.S. Geological Survey Professional Paper*: 712-B.

Chabaux, F., Bourdon, B., and Riotte, J., (2008). "U-Series Geochemistry in Weathering Profiles, River Waters and Lakes." *Radioactivity in the Environment, 13,* 50-91.

Cheng, H., Edwards, R.L., Hoff, J., Gallup, C.D., Richards, D.A., Asmerom, Y., (2000). "The Half-lives of Uranium-234 and Thorium-230." *Chemical Geology*, *169*, 17-33.

Copenhaver, S.A., Krishnaswami, S., Turekian, K.K., and Shaw, H., (1992). "^{238}U and ^{232}Th Series Nuclides in Groundwater from the H-13 Well at the Nevada Test Site: Implications For Ion Retardation." *Geophysical Research Letters, 19*(13), 1383-1386.

Dequnicey, O., Chabaux, F., Clauer, N., Sigmarsson, O., Liewig, N., and Leprun, J., (2002). "Chemical Mobilizations in Laterites: Evidence from Trace Elements and ^{238}U-^{234}U-^{230}Th Disequilibria." *Geochimica et Cosmochmica Acta, 66*(7), 1197-1210.

Deschamps, P., Hillaire-Marcel, C., Michelot, J., Doucelance, R., Ghaleb, B., and Buschaert, S., (2004). "^{234}U/^{238}U Disequilibrium Along Stylolitic Discontinuities in Deep Mesozoic Limestone Formation of the Eastern Paris Basin: Evidence for Discrete Uranium Mobility Over the Last 1-2 Million Years." *Hydrology and Earth System Sciences, 8*(1), 35-46.

Drellack, S.L Jr. and Ortego, K.P., (2007). "A Hydrostrat Model and Alternatives for Groundwater Flow and Contaminant Transport Model of Corrective Action Unit 99: Rainier Mesa-Shoshone Mountain, Nye County, Nevada." *United States Department of Energy Internal Report: National Security Technologies, LLC,* OSTI ID: 934454.

Faure, G. (1986). *Principles of Isotope Geology (2nd ed.).* New York: John Wiley & Sons.

Fenelon, J.M., Sweetkind, D.S., and Laczniak, R.J., (2010). "Groundwater Flow Systems at the Nevada Test Site, Nevada: A Synthesis of Potentiometric Contours, Hydrostratigraphy, and Geologic Structures." *U.S. Geological Survey Professional Paper, 1771*(54) 6 pls.

Gascoyne, M and Miller, N.H., (2000). "Uranium-Series Disequilibrium in Tuff and Granite: Hydrogeological Implications." *United States Department of Energy Internal Report: Office of Scientific and Technical Information,* OSTI ID: 860277.

Jaffey, A.H., Flynn, K.F., Glendenin, L.E., Bentley, W.C., and Essling, A.M., (1971). "Precision measurements of half-lives and specific activities of ^{235}U and ^{238}U." *Physical Review C, 4*, 1889-1906.

Krishnaswami, S., Graustein, W.C., Turekian, K.K., and Dowd, J.F., (1982). "Radium, Thorium, and Radioactive Lead Isotopes in Groundwaters: Application to the in Situ Determination of Adsorption-Desorption Rate Constants and Retardation Factors." *Water Resources Research, 18*(6), 1633-1675.

Lacziak, R.J., Cole, J.C., Sawyer,D.A., and Trudeau, D.A., (2005). "Summary of Hydrogeologic Controls on Ground-Water Flow at the Nevada Test Site, Nye County Nevada." U.*S. Geological Survey WRIR, 96* (4109).

Latham, A.G. and Schawrcz, H.P., (1987). "On the Possibility of Determining Rates of Removal of Uranium From Crystalline Igneous Rocks Using U-Series Disequilibria-1: A U-leach Model, and its Applicability to Whole-Rock Data." *Applied Geochemisty,2*, 55-65.

Lounsbury, M., (1956). "The Natural Abundances of the Uranium Isotopes." *Canadian Journal of Chemistry, 34*(3), 259-264.

Maher,K., DePablo, D.J., and Christensen, J.N., (2006). "U-Sr Isotopic Speedometer: Fluid Flow and Cehmical Weathering Rates in Aquifers." *Geochimica et Cosmochimica Acta, 70*, 4417-4435.

Neretnieks, I., (1980). "Diffusion in the Rock Matrix: An Important Factor in Radionuclide Retardation?" *Journal of Geophysical Research, 85*(B8), 4379-4397.

Neymark, L.A., and Paces, J.B. (2000). "Consequences of Slow Growth for ^{230}Th/U Dating of Quarternary Opals, Yucca Mountain, NV, USA. " *Chemical Geology, 164*, 143-160.

Neymark, L.A., Paces, J.B., Chipera, S.J., and Vaniman, D.T., (2006) "Uranium-Series Constraints on Subrepository Water Flow at Yucca Mountain, Nevada." *United States Department of Energy Internal Report: Yucca Mountain Project, Las Vegas, Nevada,* OSTI ID: 893804.

Osmond, J.K. and Cowart, J.B., (1992). Groundwater. In M. Ivanovich and R. Harmon (Eds.), *Uranium Series Disequilibrium: Application to Environmental Problems (2nd ed.).* Oxford: Clarendon Press.

Paces, J.B., Ludwig, K.R., Peterman, Z.E., and Neymark, L.A., (2002). "^{234}U/^{238}U Evidence for Local Recharge and Patterns of Ground-water Flow in the Vicinity of Yucca Mountain, Nevada, USA." *Applied Geochemistry, 17,* 751-779.

Paces, J.B., Neymark, L.A., Ghezzehei, T. and Dobson, P.F., (2006). "Testing the Concept of Drift Shadow at Yucca Mountain." *International High-Level Radioactive Waste Management Conference, Las Vegas, Nevada, American Nuclear Society*, 278-285.

Paces, J.B., Peterman, Z.E., Futo, K., Oliver, T.A., and Marshall, B.D., (2007). "Strontium Isotopic Composition of Paleozoic Carbonate Rocks in the Nevada Test Site Vicinity, Clark, Lincoln, and Nye Counties, Nevada, and Inyo County, California." *U.S. Geological Survey Data Series ,280*, 42 p.

Porcelli, D. and Swarzenski, P.W., (2003). "The Behavior of U- and Th-series Nuclides in Groundwater." *Reviews in Mineralogy and Geochemistry, 52*(1), 317-361.

Porcelli, D., (2008). "Investigating Groundwater Processes Using U- and Th- Series Nuclides." *Radioactivity in the Environment, 13,* 106-133.

Reiner, S.R., Laczniak, R.J., DeMeo, G.A., Smith, J.R., Elliot, P.E., Nylund, W.E., and Fridrich, C.J., (2002). "Ground-Water Discharge Determined from Measurements of Evapotranspiration, and Other Available Hydrologic Components, and Shallow Water-Level Changes, Oasis Valley, Nye County, Nevada." *United States Department of Energy Internal Report: Office of Environmental Restoration and Waste Managaement, Carson City, Nevada,* Water-Resources Investigations Report 01-4239.

Sak, P.B., Navarre-Sitchler, A.K., Miller, C.E., Daniel, C.C., Gaillardet, J., Buss, H.L., Lebedeva, M.I., and Brantley, S.L., (2010). "Controls on Rind Thickness on Basaltic Andesite Clasts Weathering in Guadeloupe." *Chemical Geology, 276*, 129-143.

Schumacher, B.A., Shines, K.C., Burton, J.V., and Papp, M.L., (1991). "A Comparison of Soil Sample Homogenization Techniques." *Hazardous Waste Measurements*. Ed. Simmons, M.S. Lewis Publishers, Inc. Boca Raton, FL. pp. 53-68.

Thiel, K., Vorwerk, R., Saager, R., and Stupp, H.D., (1983). "235U Fission Tracks and 238U-series disequilibria as a means to study recemt mobilization of Urnainum in Archaean Pyritic Congolmerates.: *Earth and Planetary Science letters, 65*, 249-262.

Tricca, A., Wasserburg, G.J., Porcelli, D., and Baskaran, M, (2000). "The Transport of U- and Th-series Nuclides in a Sandy Unconfined Aquifer." *Geochimica et Cosmochimica Acta, 65*(8), 1187-1210.

United States. Dept. of State "Limited Test Ban Treaty", Signed at Washington August 5 1963 by President John F. Kennedy.

Weis, D., Kieffer, B., Maerschalk, C., Barling, J., Williams, G.A., Hanano, D., Pretorius, W., Mattielli, N., Scoates, J.S., Goolaerts, A., Friedman, R.M., and Mahoney, J.B., (2006).

"High-Precision Isotopic Characterization of USGS reference materials by TIMS and MC-ICP-MS." *Geochemistry, Geophysics, Geosystems (G³),7*(8).

Wood, D.B., (2009). "Digitally Available Interval-Specific Rock-Sample Data Compiled From Historical Records, Nevada Test Site and Vicinity, Nye County, Nevada." *U.S. Geological Survey Data Series ,297*, 56 p.

APPENDIX: I

Shorthand classification of hydrostratigraphic units at Pahute Mesa.

BFCU	Bull Frog Confining Unit
BRA	Belted Range Aquifer
CFCU	Crater Flat Confining Unit
CHCU	Calico Hills Confining Unit
CHZCM	Calico Hills Zeolitic Composite Unit
IA	Inlet Aquifer
LPCU	Lower Paintbrush Confining Unit
TCA	Tiva Canyon Aquifer

APPENDIX: II

Chromatographic Exchange Procedure for producing purified salts of U and Th

1 ml BioRad AG 1x8 200-400 Mesh added to cleaned columns

   Wash with H_2O (3 Reservoir Volumes)

   Wash with 0.05 N HNO_3 (3 Reservoir Volumes)

   Equilibrate with 7 N HNO_3 (2 Column Volumes)

Load Samples from Hotplate as 1 ml 7 N HNO_3

   Wash with 7 N HNO_3 (4 Column Volumes)

Switch to Thorium Beakers

   Elute with 6.5 N HCl (3 Column Volumes)

   Dry down Th beakers at 105°C

   Switch to wash vats

   Wash columns with 6.5 N HCl (3 Column Volumes)

Switch to Uranium Beakers

   Elute U with 0.05 N HNO_3 (4 Column Volumes)

   Further elute U with H_2O (4 Column Volumes)

   Dry down U beakers at 105°C

Samples were then visually analyzed to determine if a second pass through columns was needed. Any beaker with any more than approximately 1 ml of a visible salt was passed through columns a second time according to the following procedure.

0.5 ml AG 1x8 200-400 Mesh BioRad added to cleaned columns

   Wash with H_2O (4 Reservoir Volumes)

   Wash with 0.05 N HNO_3 (4 Reservoir Volumes)

   Equilibrate with 0.05 N HNO_3 (2 Column Volumes)

Load Samples from hotplate as 0.5 ml 7 N HNO$_3$

> *Wash with 7 N HNO$_3$ (3 Column Volumes)*

> *Wash with 6.5 N HCl (5 Column Volumes)*

Switch to Uranium Beakers

> *Elute with 0.05 N HNO$_3$ (5 double Column Volumes)*

> *Elute with H$_2$O (2 double Column Volumes)*

> *Dry down U beakers at 105°C*

Switch to wash Vats

> *Re-equilibrate with 7 N HNO$_3$ (2 Column Volumes)*

> *Load Th beakers as 7 N HNO$_3$*

> *Wash with 7 N HNO$_3$ (4 Column Volumes)*

Switch to Thorium Beakers

> *Elute with 6.5 N HCl (3 Column Volumes)*

> *Elute with 1.0 N HCl (3 Column Volumes)*

> *Elute with H$_2$0 (2 Column Volumes)*

> *Dry down Thorium Beakers at 105°C*